

**LIGHT TRAPPING IN THIN FILM CRYSTALLINE  
SILICON SOLAR CELLS**

by

JAVANEH BOROUMAND AZAD  
B.S. Shahid Beheshti University, 2009  
M.S. University of Central Florida, 2013

A dissertation submitted in partial fulfillments of the requirements  
for the degree of Doctor of Philosophy  
in the Department of Physics,  
in the College of Sciences  
at the University of Central Florida  
Orlando, Florida

Spring Term  
2017

Major Professor: Debashis Chanda

© 2017 Javaneh Boroumand

## ABSTRACT

This dissertation presents numerical and experimental studies of a unified light trapping approach that is extremely important for all practical solar cells. A 2D hexagonal Bravais lattice diffractive pattern is studied in conjunction with the verification of the reflection mechanisms of single and double layer anti-reflective coatings in the broad range of wavelength 400 nm - 1100 nm. By varying thickness and conformity, we obtained the optimal parameters which minimize the broadband reflection from the nanostructured crystalline silicon surface over a wide range of angle  $0^{\circ}$ - $65^{\circ}$ . While the analytical design of broadband, angle independent anti-reflection coatings on nanostructured surfaces remains a scientific challenge, numerical optimization proves a viable alternative, paving the path towards practical implementation of the light trapping solar cells. A 3  $\mu\text{m}$  thick light trapping solar cell is modeled in order to predict and maximize combined electron-photon harvesting in ultrathin crystalline silicon solar cells. It is shown that the higher charge carrier generation and collection in this design compensates the absorption and recombination losses and ultimately results in an increase in energy conversion efficiency. Further, 20  $\mu\text{m}$  and 100  $\mu\text{m}$  thick functional solar cells with the light trapping scheme are studied. The efficiency improvement is observed numerically and experimentally due to photon absorption enhancement in the light trapping cells with respect to a bare cell of same thickness.

*To Imen, who is the love of my life*

## ACKNOWLEDGMENTS

This work at University of Central Florida was partially supported by the National Science Foundation grant no # 63016055, for which I am thankful.

I acknowledge the support and guidance for this dissertation committee's chair, Dr. Debashis Chanda, during the past three years that I have worked on this group which I appreciate.

I wish to express my sincere gratitude to Prof. Robert Peale for his continuous support and mentorship not only during the first three years of my PhD as my major advisor but through the end of my journey as a PhD candidate. He showed me what it means to be a professional scientist. I am deeply grateful for having such a reliable mentor in my life.

I would like to thank Dr. Schoenfeld, Prof. Enrique Del Barco, and Dr. Elena Flitsiyan for their guidance and accepting to be on my dissertation committee.

I acknowledge my colleagues for their support, Abraham Vázquez-Guardado, Daniel Franklin, Alireza Safaei, Dr. Evan Smith, Pedro Figueiredo, Dr. Janardan Nath, Dr. Farnood Rezaie, Dr. Deep Panjwani, Doug Maukonen, and Chris Fredricksen. Additionally I would like to acknowledge Dr. Schoenfeld's group, Dr. Kristopher Davis, Dr. Eric Schneller, Dr. Ngwe Zin, and Sara Bakhshi, for all of their helps in this research.

I am grateful to my kind parents, my mom, Mrs. Ozra Mohebbi who unconditionally loves me for who I am and always supported me to pursue higher education and my father, Javad Boroumand Azad, who taught me to be a hard worker and be determined to reach my goals. I acknowledge supports of my beloved grandma, brother, and sister who are always in my thoughts for their kindness and support.

Most importantly I would like to express my sincere appreciation to my beloved husband, Imen Rezadad, who is being the best friend and colleague I could ever ask for. I acknowledge his great help in the first phase of my research as a colleague and his kind endless support, friendship and love in all levels of hardship in my life.

At last but not least, I would like to thank the chair of Physics department, Dr. Eduardo Mucciolo, and all great staff in Physics department at UCF for supporting me to finish my PhD in good spirits.

# TABLE OF CONTENTS

LIST OF FIGURES .....	x
LIST OF TABLES .....	xv
CHAPTER 1 INTRODUCTION.....	1
1.1 Photovoltaics Overview .....	1
1.2 Solar Cell Fundamentals .....	2
1.2.1 Sun Power .....	2
1.2.2 Semiconductor Characteristics.....	3
1.2.2.1 Materials Attribute.....	3
1.2.2.2 Equilibrium Carrier Concentration .....	4
1.2.2.3 Generation, Recombination and Lifetime .....	6
1.2.2.4 Carrier Transport (Drift and Diffusion Current).....	9
1.2.2.5 P-N Junction .....	11
1.2.3 Solar Cell Characteristics.....	12
1.2.3.1 Short-circuit Current.....	13
1.2.3.2 Open-circuit Voltage .....	14
1.2.3.3 Fill Factor .....	14
1.2.3.4 Efficiency.....	14
1.2.3.5 Quantum Efficiency.....	15

1.3	Light Trapping in Thin Film Solar Cells.....	15
1.3.1	Background.....	15
1.3.2	Periodic Light Trapping Nano-Structures.....	19
1.3.3	Large Area Nanoscale Patterning .....	21
1.3.4	Design, Optimization, and Fabrication .....	22
1.4	Dissertation Outline.....	27
CHAPTER 2 BROADBAND ANGLE INDEPENDENT ANTI-REFLECTION COATINGS ON NANOSTRUCTURED LIGHT TRAPPING SOLAR CELLS .....		29
2.1	Introduction .....	29
2.2	Results and Discussion.....	30
2.3	Methods.....	40
2.3.1	Fabrication .....	40
2.3.2	Optical Measurements and Imaging .....	40
2.3.3	Modeling.....	41
2.4	Conclusion.....	41
CHAPTER 3 UNIFIED ELECTROMAGNETIC-ELECTRONIC DEVICE DESIGN		43
3.1	Introduction .....	43
3.2	Results and Discussion.....	44
3.2.1	Light Trapping c-Si Solar Cell Optical Responses .....	44



3.2.2	Electronic Device Modeling .....	51
3.2.3	Device Optimization and Simulation Parameters .....	58
3.3	Methods .....	62
3.4	Conclusion.....	65
CHAPTER 4 FUNCTIONAL LIGHT TRAPPING CELLS .....		67
4.1	Introduction .....	67
4.2	Results and Discussion.....	68
4.3	Methods .....	77
4.3.1	100 $\mu\text{m}$ Cell Fabrication .....	77
4.3.2	20 $\mu\text{m}$ Cell Fabrication .....	79
4.4	Conclusion.....	82
CHAPTER 5 CONCLUSION .....		84
LIST OF REFERENCES .....		87

## LIST OF FIGURES

Figure 1-1 shows the I-V diagram of a solar cell in dark and under illumination .....	12
Figure 1-2 illustrates a simplified form of a solar cell circuit.....	13
Figure 1-3 shows the incident light path through a bulk semiconductor (a), with a rear side reflector (b), when top surface texturing is added (c), ARCs further reduce the reflectance. ....	18
Figure 1-4 shows cross section schematic view of an incident beam creating forward and backward diffraction modes at a 2D periodic grating interface.....	20
Figure 1-5 (a) shows the fabricated pattern on a master by using DLW technique, (b) then the pattern is transferred onto PDMS mold, (c) that can be used for imprinting repeatedly. ....	22
Figure 1-6 FDTD predicted light trapping pattern optimization for a constant silicon thickness (3 $\mu\text{m}$ ). The wavelength integrated absorption is maximized as a function of 2D hexagonal lattice period, D/P and relief depth ( $P = 500 \text{ nm}$ , $D/P = 0.6$ , $RD = 140 \text{ nm}$ with ARC ( $\text{SiO}_2/\text{Si}_3\text{N}_4 = 50/35 \text{ nm}$ , chosen from previous work) and 200 nm Au as BSR. ....	23
Figure 1-7 (Left to right) top, tilted and cross section view SEM images of fabricated silicon nanostructures as a 2D periodic hexagonal grating.....	24
Figure 1-8 (a-c) illustrate the fabrication steps for Soft imprinting from PR spin coating and baking (a), imprinting, UV exposure followed by post exposure baking (b), removing PR residues by $\text{O}_2$ plasma etching (c), to MaCEtch process (d-f) including metal deposition (d), etching silicon in $\text{H}_2\text{O}_2:\text{HF}:\text{HO}_2$ solution (e) and removing the PR (f)....	25

Figure 1-9 (a) shows a SEM image of silicon nanostructures cross section that is etched with MaCEtch technique. (b) shows the experimentally obtained etch rate of silicon at Si/Au interface with 0.5 ml and 1 ml H<sub>2</sub>O<sub>2</sub> concentrations in (H<sub>2</sub>O<sub>2</sub>:HF:HO<sub>2</sub>) solution.. 27

Figure 2-1(a) shows the top and side view SEM images of the bare and ARC coated 2D grating fabricated by using metal assisted chemical etching technique. (b) shows interdigitated back contact solar cell architecture with the light trapping scheme as an application of such angle independent light-trapping nanostructures..... 31

Figure 2-2 (a) reflectance as a function of wavelength and thickness for three single layer ARCs for nanostructure period 500 nm, relief depth 140 nm and diameter 320 nm. White lines indicate the thickness that gives the minimum reflectance. (b) compares the reflectance vs wavelength of bare silicon (magenta dash line), patterned silicon (magenta), and patterned Si coated with Al<sub>2</sub>O<sub>3</sub> (red), SiO<sub>2</sub> (black) and Si<sub>3</sub>N<sub>4</sub> (blue) conformal with the thicknesses indicated with white dash lines in (a). (c) compares the wavelength integrated reflectance as a function ARC thicknesses for bare (dash) and patterned silicon (solid)..... 32

Figure 2-3 (a) schematic of step coverage of a silicon post coated with single layer ARC. (b-d) A comparison of reflectance vs wavelength of Al<sub>2</sub>O<sub>3</sub> (a), Si<sub>3</sub>N<sub>4</sub> (b), and SiO<sub>2</sub> (c) coatings with 20%, 60%, and 100% step coverages. .... 34

Figure 2-4 (a) reflectance over a broadband wavelength regime (400- 1100 nm) for three single layer non-conformal antireflection coatings. The dots indicate the thicknesses at which the measured reflectance spectra is matched with the equivalent predicted one for Al<sub>2</sub>O<sub>3</sub> (b), Si<sub>3</sub>N<sub>4</sub> (c), and SiO<sub>2</sub> (d)..... 36

Figure 2-5 (a) shows predicted wavelength integrated reflectance as a function of Si<sub>3</sub>N<sub>4</sub>-SiO<sub>2</sub> bilayer ARC thickness for conformal and non-conformal coatings on patterned silicon. The optimum ARC thicknesses at which the minimum reflection is obtained are marked as star. (b) presents experimentally measured and predicted reflectance vs wavelength for non-conformal 70 nm Si<sub>3</sub>N<sub>4</sub>- 100 nm SiO<sub>2</sub> bilayer coatings are in a good agreement..... 38

Figure 2-6 compares predicted and experimentally measured angle resolved reflectance from the optimized ARC coated patterned silicon..... 39

Figure 3-1 illustrates the c-Si solar cell architecture which combines the light trapping scheme with the functional cell geometry. .... 45

Figure 3-2 shows the absorbed photo flux as a function of wavelength with reference to AM1.5D solar spectrum for bare and light trapping cell inside a 3 μm thick wafer. .... 46

Figure 3-3 shows the corresponding band diagram under illumination. .... 47

Figure 3-4 shows silicon absorption as a function of silicon thickness for the optimized light trapping pattern (P = 500 nm, D/P = 0.6, RD = 140 nm with ARC (SiO<sub>2</sub>/SiN = 50/35 nm), and 200 nm Au as BSR) vs bared silicon. .... 48

Figure 3-5 compares the FDTD predicted absolute absorption inside 3 μm thick bare and light trapping cells..... 49

Figure 3-6 illustrates the power absorbed per unit volume in 3 μm thick bare and light trapping cell at strong (λ = 461 nm) and weak (λ = 977 nm) absorbing regimes. .... 49

Figure 3-7 compares the wavelength integrated charge carrier generation rate (g) over a 2D plane across the center of the hexagonal unit cell..... 50

Figure 3-8 (a) shows the doping profile of the 3  $\mu\text{m}$  thick silicon cell with and without light trapping. The p and n regions are defined which show the gradient of impurities in the device. (b) compares the electron density of a 3  $\mu\text{m}$  bare cell with light trapping cell. The electron density in n-type region of the light trapping cell is higher than that of the bare cell, and (c) shows the corresponding electron current density. The structure geometries in this figure are not to scale. The color bar upper and lower limits are chosen in order to enhance the contrast. .... 52

Figure 3-9 (a-b) present the predicted short circuit current density ( $J_{sc}$ ) and open circuit voltage ( $V_{oc}$ ) as a function of surface recombination velocity in the top and bottom graphs respectively, and (c-d) show the predicted short circuit current density as a function of doping concentration for both bare and light trapping cells..... 54

Figure 3-10 (a) and (b) compare the Auger and Shockley-Read-Hall recombination in bare and light trapping cells, respectively. Light trapping cell possesses higher recombination due to higher localized doping concentration and defect density. The cell geometry is not to scale..... 57

Figure 3-11 shows the corresponding I-V curves of fabricated, simulated and optimized 3  $\mu\text{m}$  bare and light trapping solar cells. .... 61

Figure 3-12 shows the fabrication process of making 3  $\mu\text{m}$  thick micro-bar solar cell on  $\langle 111 \rangle$  silicon wafer from the beginning (top left) to the end (bottom right). The direction to follow the process is shown with an arrow in the first row. .... 64

Figure 3-13 shows a SEM image of under-cut silicon microbars (left) and an optical image of transfer printed microbars onto a glass substrate (right)..... 65

Figure 4-1 shows light trapping c-Si solar cell architecture of 100 $\mu\text{m}$ (a) and (b) 20 $\mu\text{m}$ cell that is fabricated on a silicon-on-insulator (SOI) wafer.....	69
Figure 4-2 illustrates the comparison between the integrated absorption of 20 $\mu\text{m}$ c-Si solar cell with and without light trapping with respect to the solar spectrum. ....	70
Figure 4-3 presents external quantum efficiency measurement of a 100 $\mu\text{m}$ bare and patterned cell, both with ARC and BSR. ....	71
Figure 4-4 presents the impact of bulk lifetime on $J_{sc}$ (a) $V_{oc}$ (b) and $\eta$ (c) in 100 $\mu\text{m}$ cell. (d) Predicted $V_{oc}$ and $\eta$ vs bulk lifetime for 20 $\mu\text{m}$ cell verifies the results in (a).....	73
Figure 4-5 presents the I-V curves of experimental (solid lines) and predicted data (dash lines) for a 100 $\mu\text{m}$ bare (black) and a patterned solar (red) cell.....	74
Figure 4-6 presents the I-V curves of experimental (solid lines) and predicted data (dash lines) for a 20 $\mu\text{m}$ bare (black) and a patterned solar (red) cell.....	75
Figure 4-7 shows the fabrication process of making 100 $\mu\text{m}$ solar cell on $\langle 100 \rangle$ p-doped double side polished Si wafer from the beginning (top left) to the end (bottom right). The direction to follow the process is shown with an arrow in the first row. ....	79
Figure 4-8 shows the fabrication process of making 20 $\mu\text{m}$ solar cell on SOI wafer from the beginning (top left) to the end (bottom left). The direction to follow the process is shown with an arrow in the first row. ....	81
Figure 4-9 (left) shows the fabricated 20 $\mu\text{m}$ solar cell on SOI wafers, (right) shows the flexibility of a thin Si. ....	82

## LIST OF TABLES

Table 3-1 The electrical simulation parameters of the fabricated (Sim.) and optimized (Opt.) bare and light trapping cells .....	59
Table 3-2 Short circuit current ( $J_{sc}$ ), open circuit voltage ( $V_{oc}$ ), fill factor (FF), and efficiency ( $\eta$ ) of fabricated, simulated and optimized 3 $\mu\text{m}$ bare and light trapping solar cells .....	60
Table 4-1 Short circuit current ( $J_{sc}$ ), open circuit voltage ( $V_{oc}$ ), fill factor (FF), and efficiency ( $\eta$ ) of fabricated and optimized 100 $\mu\text{m}$ bare and patterned solar cells.....	74
Table 4-2 Short circuit current ( $J_{sc}$ ), open circuit voltage ( $V_{oc}$ ), fill factor (FF), and efficiency ( $\eta$ ) of fabricated and optimized 20 $\mu\text{m}$ bare and patterned solar cells.....	75
Table 4-3 The electrical simulation parameters of the optimized (Opt.) bare and patterned solar cells .....	76
Table 4-4 The lifetime measurement results for 100 $\mu\text{m}$ and 200 $\mu\text{m}$ c-Si wafers. ....	77

# CHAPTER 1 INTRODUCTION

## 1.1 Photovoltaics Overview

Photovoltaic (PV) is the effect of converting light into electricity by using solar cells. When light exposes a semiconductor material, absorbed photons generate electron-hole (e-h) pairs which are directed to negative and positive terminals of the cell. This happens when a photon with energies equivalent or higher than the material's bandgap energy is applied to the valence band and excite a weakly bonded electron to the conduction band that is a higher energy level which results in electric conduction through the material. The generated electricity is collected from the metal electrodes using an external load.

Photovoltaic effect was first discovered by a French physics, Becquerel, while experimenting with metal electrodes in an electrolyte in 1839. In 1877, Adams and Day observed that the radiated selenium electrodes produced electricity. In 1904, Albert Einstein explained the theory of the phenomenon behind PV effect which was experimentally proven by Robert Millikan in 1916. Decades after discovery of Jan Czochralski's method to grow monocrystalline silicon, Bell's laboratories announced their achievement of inventing the crystalline first silicon solar cell with 6% efficiency in 1954<sup>1</sup>. The first application of solar cells was to power space satellites. In 1985, 20% efficiency was achieved from silicon solar cells<sup>2</sup>. Since then the photovoltaic industry focused on high efficiency solar cells to reduce the cost of manufacturing. Low cost and high efficiency solar cells are important in order to reduce the fossil fuel based power generation and minimize environmental pollution. Nowadays, solar cell modules are being used for grid and off-grid power generation in a wide range of applications such as



signal stations, transportation, telecommunication, building integrated systems, space, etc.<sup>1,3</sup> Although, green power generation is still more expensive than fossil fuel usage and renewable energy suffers from lack of economical energy storage, many governments are perusing the solar power technology improvement due to the climate change moderation.

There are different types of solar cells such as single junction<sup>4,5</sup>, multi-junction<sup>6</sup>, organic<sup>7</sup>, perovskite<sup>8</sup>, plasmonic<sup>9</sup>, dye-sensitized<sup>10</sup>, hybrid<sup>11</sup>, tandem<sup>12</sup>, and many other in order to growth solar industry.

## 1.2 Solar Cell Fundamentals

### 1.2.1 Sun Power

The total power density emitted from a blackbody (e.g. sun) is determined from integrated spectral irradiance that is given by Plank's law over all wavelengths. The wavelength at which the spectral irradiance is at maximum is given by  $\lambda$  ( $\mu\text{m}$ ) =  $2900/T$  where T is the blackbody temperature in Kelvin. The intensity of the solar irradiance in free space is  $1.35 \text{ KW/m}^2$  when the sun radiation is at normal angle of incident which is also known as air mass zero (AM0) where the air mass is a measure of light power intensity from the free space to the earth surface. As the light passes through the atmosphere, the particles on its way in the atmosphere such as ozone, carbon dioxide, and water vapor absorb about 28% the light in the ultraviolet and infrared wavelength regime while dust particles scatter about 10% of the light that is also known as diffuse light. The air mass number is given by Air mass =  $1/\cos \theta$  where  $\theta$  is the angle of incidence ( $\theta = 0$  when the sun is directly overhead)<sup>13</sup>. AM1.5G (global) spectrum includes the diffuse light

whereas AM1.5D (direct) doesn't. The angle between the sun rays to the earth surface differs from normal ( $90^\circ$ ) to parallel ( $0^\circ$ ) which depends on the position of a fixed point earth, day of the year, and time of the day. At normal angle, the light intensity is at its maximum ( $1 \text{ kW/m}^2$ ).

## 1.2.2 Semiconductor Characteristics

### 1.2.2.1 Materials Attribute

The vast majority of solar cells are made from semiconductors in periodic table, group IV (e.g. crystalline silicon (c-Si)) or of combinations from groups II-VI and III-V (e.g. Cadmium Telluride (CdTe) and Gallium Arsenide (GaAs) respectively). Atomic properties of the semiconductors determine their optical and electronic properties. Group II-VI and II-V semiconductor atoms are formed in a zincblende lattice, whereas group IV semiconductor atoms are arranged in a diamond lattice all of which can be represented by two interpenetrating face-centered-cubic (fcc) lattices. In diamond lattice, all the four atoms are the same while in a zincblende lattice, e.g. GaAs, one sub-lattice is gallium than the other one is Arsenic.

Semiconductors have relatively narrow energy band gaps which put the electrons in a favorable state to easily be excited by sufficient photon energy or an external electric field or voltage bias. The band gap ( $E_G$ ) is minimum energy to break the electron bonds in the valence band energy level ( $E_V$ ) and be excited to the conduction band ( $E_C$ ) where is a free energy state. On the other hand, when an electron is set free a hole is created which also play an equivalent role in the current generation. The band structure of a crystalline

solid and hence the energy-momentum (E-k) relationship can be obtained from Schrodinger equation which can be approximated near the valence and conduction band edges to  $E = \frac{\hbar^2 k^2}{2m^*}$  where  $m^*$  is the effective mass and  $k$  is related to the lattice constant

(a). When the maximum of the valence band and the minimum of the conduction band occur at the center of k-space which gives the same crystal momentum the semiconductor is a direct band gap, e.g. GaAs. In contrast, the minimum of the conduction band is misaligned with the maximum of the conduction band, in an indirect band gap semiconductor, e.g. Si, which requires a higher energy level than its band gap energy for a direct transition. However, this change in their momentum can be compensated by thermal vibrations in the lattice (phonons) which have very high momentum despite their low energy.

#### 1.2.2.2 Equilibrium Carrier Concentration

Semiconductor without any additional impurities (undoped) is called intrinsic material,  $n_i$ , which is a function of bandgap energy and temperature. In thermal equilibrium the number of electrons in the conduction band ( $n_0$ ) is equal to the number of holes in the valence band ( $p_0$ ). Then we have<sup>14</sup>:

$$p_0 n_0 = n_i^2 = N_C N_V e^{(E_V - E_C)/kT} = N_C N_V e^{-E_G/kT} \quad (1)$$

Where  $N_C$  and  $N_V$  are the effective densities of state (number/cm<sup>3</sup>),  $k$  is Boltzmann's constant, and  $T$  is the Kelvin temperature. Intrinsic semiconductor's carrier concentration is several orders of magnitude lower than the semiconductors with impurities (e.g.  $n_i \approx 10^{10} \text{ cm}^{-3}$  in Si).

Conductivity of semiconductors can be controlled by introducing impurities, called dopants, into the semiconductor atoms. N-type semiconductor is created when group IV materials are doped with group V atoms (e.g. Silicon doped with phosphorous) while p-type semiconductor is created when group IV materials are doped with group III atoms (e.g. Silicon doped with boron). Since n-type materials (e.g. phosphorous) have five valence electrons, four of which can bond with silicon atoms, the extra electron is donated to the conduction band. An extra hole is left behind when silicon doped with p-type materials (e.g. boron). The holes in the n-type and electrons in p-type semiconductor are considered to be the minority carriers. When a photon with  $\geq E_G$  get absorbed by the semiconductor it generates both majority and minority carriers. However, since the number of majority carriers already exists in the semiconductor due to doping of orders of magnitude more than the number of light generated carriers, illumination doesn't impact this number as it does for the minority carriers. In contrast, due to very small concentration of minority carriers in the dark, the number of light generated minority carrier in the illumination can be approximated as the total number of minority carriers. Below equation gives the majority and minority carrier concentrations:

$$n - \text{type: } n_0(\text{or } n_n) = N_D, \quad p_0(\text{or } p_n) = \frac{n_i^2}{N_D} \quad (2)$$

$$p - \text{type: } p_0(\text{or } p_p) = N_A, \quad n_0(\text{or } n_p) = \frac{n_i^2}{N_A} \quad (3)$$

where  $N_D$  and  $N_A$  are the concentration of donor and acceptor atoms. As the doping concentration increases the minority carrier concentration decreases according to above equation. When the dopant concentration is very large the bandgap is reduced and as a

result the intrinsic carrier concentration is increased. This effect is called bandgap narrowing which is managed to avoid in solar cells. This work considers that all dopant atoms are ionized when introduced into the semiconductor at room temperature.

### 1.2.2.3 Generation, Recombination and Lifetime

Absorbing photons when with sufficient energy to excite electrons to the conduction band (larger than the band gap of semiconductor), depends on the material and the wavelength of incident light which can be defined as absorption coefficient that is given by  $\alpha = \frac{4\pi\kappa}{\lambda(nm)}$  where  $\kappa$  is the extinction coefficient. The absorption depth in a semiconductor is also defined by the inverse of the absorption coefficient which determines how deep the light can travel inside the semiconductor before 64% of it gets absorbed. As the light (photon) absorption occurs, the electron hole pair generation takes place. The rate of which (G) is given by<sup>14</sup>:

$$G = \alpha N_{ph} = \alpha N_{ph0} e^{-\alpha x} \quad (4)$$

where  $N_{ph}$  is the photon flux (photons/unit area/second),  $N_{ph0}$  is the photon flux at the surface and  $x$  is the distance into the material from the surface. By integrating the photon flux over a wavelength range, G becomes:

$$G = \int_{\lambda_{min}}^{\lambda_{max}} \alpha(\lambda) N_{ph}(\lambda) d\lambda \quad (5)$$

This formula is used in our modeling which is going to be discussed in the following chapters.

The carrier generation has a reverse process called recombination which occurs when an excited electron from the conduction band stabilize in a lower energy level (i.e. recombine with a hole in the valence band). For intrinsic semiconductor this rate is equivalent with the generation rate in order to maintain their thermal equilibrium. In solar cells though, this is the main source of loss. There are three main recombination mechanisms which play an important role in the solar cells, Radiative (band-to-band), Auger, and Shockley-Read-Hall (defect level) recombination.

Radiative recombination is dominant in direct band gap semiconductors where an electron directly recombines with a hole which leads to a photon emission with an energy close to the band gap. Radiative recombination is defined by<sup>14</sup>:

$$R_r = B(pn - n_i^2) \quad (6)$$

where B is the radiative recombination coefficient ( $4 \times 10^{-31} \text{ cm}^6 \text{ s}^{-1}$ ). This type is very weak in an indirect band gap semiconductor such as silicon so it is usually neglected.

Auger recombination occurs when an electron recombines with a hole and the released energy is given to a second electron in the conduction band (or hole in the valence band) which then thermally relaxes back to its previous position. This process is dominant in heavily doped semiconductors or under high injection conditions (e.g. concentrator solar cells) and is calculated from<sup>14</sup>:

$$R_A = (C_{p0}p + C_{n0}n)(np - n_i^2) \quad (7)$$

where  $C_{p0}$  and  $C_{n0}$  are auger recombination coefficients which are proportional to the inverse quadratic carrier concentration at high doping levels. The first term is dominant in

a p-type material and the second term is dominant in an n-type material. In high level injection or heavily doped p-n junction both terms are important.

Shockley-Read-Hall (SRH) recombination is dominant in semiconductors with defects in their crystal lattice. It occurs when an electron and a hole are trapped in an energy level in the forbidden gap that is introduced through defects. It is more likely with energy levels near mid-gap and is given by<sup>14</sup>:

$$R_{SRH} = \frac{np - n_1 p_1}{\tau_{p0}(n + n_1) + \tau_{n0}(p + p_1)} \quad (8)$$

where  $\tau_{p0}$  and  $\tau_{n0}$  are which inversely depend on the carrier thermal velocity ( $10^7$  cm/s at 300 K), density of defects and electron and hole capture cross-section ( $10^{-15}$  cm<sup>2</sup>) and  $n_1(p_1) = n_i \exp(\pm E_t \mp E_i/kT)$  where  $E_t$  is the energy of the defect level. In mono-crystalline silicon solar cells the SRH recombination is the dominant recombination.

Recombination rate depends on the minority carrier lifetime and the number of excess minority carriers noted as  $R = \Delta n/\tau$  in the low level injected ( $\Delta p = \Delta n \ll N_D, N_A$ ) semiconductors.

The minority carrier lifetime is the average time in which an excited electron at the conduction band spends before recombining with a hole. In above equation, R is the combination of all three recombination; hence the lifetime in the bulk of a semiconductor is given by<sup>15</sup>:

$$\frac{1}{\tau_{bulk}} = \frac{1}{\tau_{Band}} + \frac{1}{\tau_{Auger}} + \frac{1}{\tau_{SRH}} \quad (9)$$

The longer lifetime semiconductor results in a higher efficiency solar cell. The lifetime of a carrier after generation indicates the average length it can travel in the semiconductor

before it recombines. These two factors are related as  $L = \sqrt{D\tau}$  where  $D$  is the diffusivity ( $\text{m}^2/\text{s}$ ).

Apart from the bulk recombination probabilities, the surface of a semiconductor is also a site of high recombination due to the abrupt cut-off of the crystal lattice at the surface that is called surface recombination and it is characterized by a term called “surface recombination velocity” in  $\text{cm}/\text{s}$ . The minimum value of this term is zero for an ideal surface with no recombination while the maximum velocity goes to  $10^7$   $\text{cm}/\text{s}$  for most of semiconductors. A surface passivation process can lower the recombination by growing a layer to bond with the dangling bonds. For simplicity, the surface recombination rate is described for n-type and p-type semiconductors respectively by<sup>14</sup>:

$$R_s = S_p(p - p_0) \quad (10)$$

$$R_s = S_n(n - n_0) \quad (11)$$

where  $S_p$  and  $S_n$  are effective surface recombination velocities.

#### 1.2.2.4 Carrier Transport (Drift and Diffusion Current)

In thermal equilibrium the drift and diffusion currents must cancel each other out in order to maintain zero net current.

When an electric field is applied in a doped semiconductor, it generates drift current due to upward band bending in the direction of the field that is controlled by majority carriers, i.e. electrons in n-type semiconductors and holes in p-type semiconductors. Electrons sink down the hill in the opposite direction of the electric field



while holes float up the hill in the same direction as the field. These free carriers in the semiconductor collide with other objects such as the atoms of crystal, dopant ions, defects and are scattered which means their velocity goes to zero and then accelerate again. As a result, the carriers move with a constant average velocity called drift velocity that is in the direction of the electric field,  $|\vec{v}_d| = |\mu\vec{E}|$ , where  $\mu$  is the magnitude of the mean drift velocity that is called carrier mobility which is mainly due to the lattice scattering and impurity scattering. Thus, the drift current density for electrons and holes is given by<sup>14,15</sup>

$$J_{n,p} = q\mu_{n,p}(n,p)\vec{E} \quad (12)$$

In the absence of external electric field, electrons and holes flow from higher concentration areas to lower concentration areas through their random motion in order to reach the concentration uniformity. This flux can be defined by the Fick's law from which diffusion current density of electron and holes is obtained

$$J_{n,p} = \pm qD_{n,p} \frac{d\Delta(n,p)}{dx} \quad (13)$$

where  $D_{n,p}$  is the electron and hole diffusion coefficient (or diffusivity) respectively. The relation between the carrier diffusion coefficients and their mobility is known as the Einstein relation,

$$D_{n,p} = \frac{\mu_{n,p}}{q} kT \text{ (cm}^2/\text{s)} \quad (14)$$

The total electron and hole current generated by both applied electric field and concentration gradient is,

$$J_n = q\mu_n nE + qD_n \nabla n \quad (15)$$

$$J_p = q\mu_p pE - qD_p \nabla p \quad (16)$$

$$J_{total} = J_n + J_p \quad (17)$$

The operation of semiconductor devices, in particular solar cells, can be addressed with three equations<sup>16</sup>, transport equations which are discussed above, Poisson's equation that describes the relationship between charge carriers and electric field strength, and the carrier continuity equations which express the relationship between carrier generation, recombination and transport within the semiconductor.

#### 1.2.2.5 P-N Junction

P-N junction is formed when an n-type and a p-type semiconductor merge with each other within the same lattice. In this case, electrons diffuse from the n-type region into the p-type region and the inverse is true for holes. This charged region is known as depletion region or space charge region. During this motion, diffused electrons and holes leave behind exposed charge impurities that are fixed in the crystal lattice and produce an electric field from positive to negative charge (from n-type to p-type) which create a drift current as oppose to the diffusion current in order to reach equilibrium condition. This is called build-in voltage (potential),  $V_{bi}$  that is the barrier height for any current to flow which can be reduced by applying a forward bias or under illumination.

### 1.2.3 Solar Cell Characteristics

The current-voltage (I-V) characteristic of a solar cell under illumination is given by the Shockley solar cell equation<sup>15</sup>

$$I = I_{ph} - I_0 \left( e^{\frac{qV}{kT}} - 1 \right) \quad (18)$$

where  $I_{ph}$  is the photo-generated current, and  $I_0$  is the dark saturated current, also known as saturated current that can be obtained by solving continuity equation.

The comparison between the I-V characteristics of an unilluminated and illuminated solar cell is shown in Figure 1-1 which is the superposition of the diode in the dark with the photo-generated current.

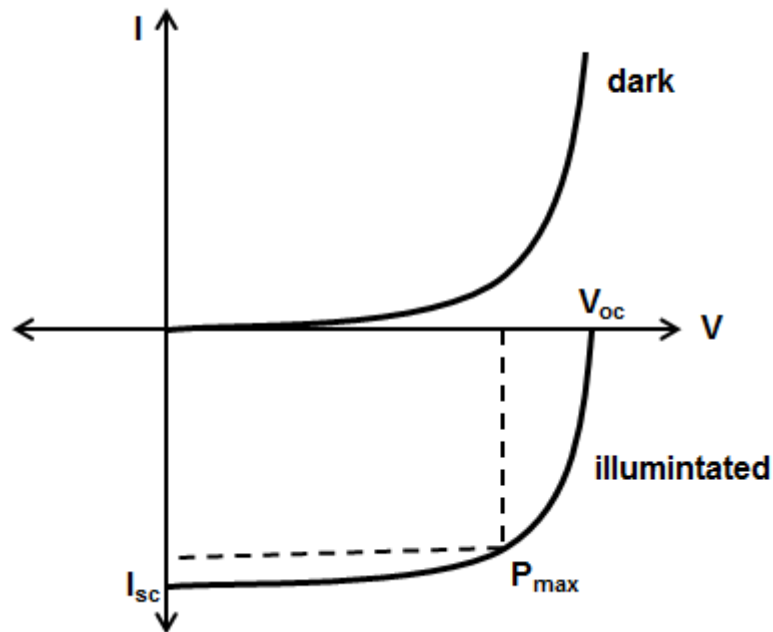


Figure 1-1 shows the I-V diagram of a solar cell in dark and under illumination

Figure 1-2 represents the simplified equivalent circuit of the cell which includes the photo-generated current, dark saturated current and the series and shunt resistances. Ohmic resistance is another loss factor in a solar cell device performance that can be divided into series and shunt resistances as the most common resistances. The series resistance existence is due to a) contact resistance at metal semiconductor interface b) ohmic resistance of both metal electrodes, and c) ohmic resistance through the emitter and base of the solar cell. The slope of the I-V curve at open circuit voltage is a good estimation of series resistance. The shunt resistance presence is due to the leakage current from the solar cell junction which depends on the manufacturing defects. These two resistances are the main cause of voltage loss and low fill factor in the solar cell.

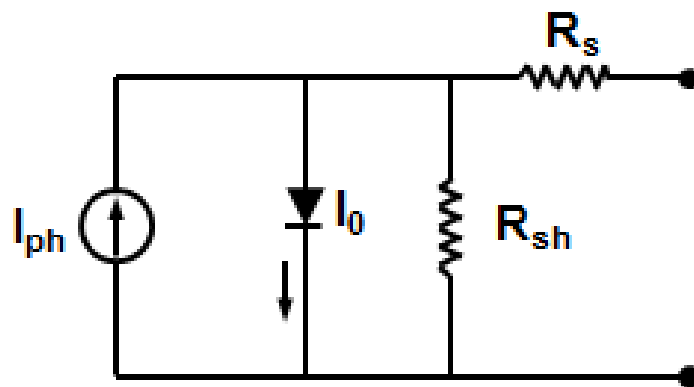


Figure 1-2 illustrates a simplified form of a solar cell circuit

### 1.2.3.1 Short-circuit Current

Short circuit current,  $I_{sc}$ , is the collected current when the voltage across the solar cell is zero, i.e. when the solar cell is short circuited and is equal to photo-generated current.

### 1.2.3.2 Open-circuit Voltage

The open circuit voltage,  $V_{oc}$ , is the maximum voltage across the solar cell when there is no current which corresponds to the bias at solar cell junction due to the photo-generated current and it is given by<sup>15</sup>

$$V_{OC} = \frac{nkT}{q} \ln\left(\frac{I_{ph}}{I_0} + 1\right) \quad (19)$$

This equation shows the dependency of  $V_{OC}$  on the dark saturated current that depends on the recombination in the cell.

### 1.2.3.3 Fill Factor

Fill factor is the ratio of the maximum achievable output power to the maximum current times maximum voltage.

$$FF = P_{max}/I_{sc}V_{oc} \quad (20)$$

It graphically represents the rectangular area underneath the I-V curve that is filled by the  $I_m \cdot V_m$  with respect to  $I_{sc} \cdot V_{oc}$ .

### 1.2.3.4 Efficiency

Efficiency is the most convenient factor to reflect the solar cell performance. It is defined as the ratio of the power output from the solar cell to incident energy input

$$\eta = \frac{P_{max}}{P_{in}} = \frac{FF I_{sc} V_{oc}}{P_{in}} \quad (21)$$

### 1.2.3.5 Quantum Efficiency

Quantum efficiency gives the current that is generated through the solar cell under illumination. It can be divided into two types, external quantum efficiency (EQE) and internal quantum efficiency (IQE). EQE is defined by the ration of the number of charge carriers collected by the solar cell to the number of incident photons whereas IQE is the ratio of EQE to the absorption of the light or in other words the ratio of the number of collected carriers to the number of absorbed photons from the incident light. Following losses cause reduction in the quantum efficiency of most solar cells: front surface reflection, front/rear surface recombination and reduced absorption, and low diffusion length, which is the average distance a carrier travel between the generation and recombination and is given by  $L = \sqrt{D\tau}$ . Here D is diffusivity as shown in equation. (14) and  $\tau$  is the carrier lifetime.

## 1.3 Light Trapping in Thin Film Solar Cells

### 1.3.1 Background

Thin (<100  $\mu\text{m}$ ) and ultra-thin (<20  $\mu\text{m}$ ) solar cells are highly attractive in the industry due to less material consumption and their mechanical flexibility when mounted on plastic substrates. The early mono-crystalline silicon solar cells approached the theoretical limit with the typical thickness of 300  $\mu\text{m}$  for which the open-circuit voltage, that is the inversely proportional to the cell thickness<sup>14</sup>, of 741 mV was the theoretical limit under one sun illumination. More recent silicon solar cells consume less material with the cell thickness of  $\sim 200 \mu\text{m}$  but are still thick enough to absorb most of the

incident light from one sun. As the PV industry moves toward thin and ultra-thin solar cells, the need for advanced light trapping structures becomes more critical.

Mono-crystalline silicon is extensively used in photovoltaic technology due to its natural abundance, excellent electronic properties, fairly matched absorption characteristics with solar spectrum, chemical/radiation hardness, low cost in manufacturing, etc. Therefore the focus of this work is on mono-crystalline silicon solar cells.

Beer Lambert law describes the absorption in semiconductors as

$$A = I_0(1 - e^{-\alpha L}) \quad (22)$$

where  $I_0$  is the incident light intensity,  $\alpha$  is the absorption coefficient and  $L$  is light path length inside the semiconductor, according to which  $L$  has to be large for small  $\alpha$  in order to have sufficient absorption.

Thinning the silicon solar cell causes an absorption loss near the band edge which corresponds to its absorption depth ( $\propto 1/\alpha$ ). Hence the efficiencies decrease significantly for thicknesses  $<20 \mu\text{m}$ . In order to maximize the charge carrier generation in a semiconductor device, that semiconductor needs to absorb as many photons as possible from the incident light, e.g. in crystalline silicon, this requires a millimeter thick material. Light trapping becomes important when silicon thickness is not enough to absorb  $>90\%$  of the light. This is defined when the light path length is larger than the absorber medium thickness when the incident light is scattered due to a textured interface in conjunction with anti-reflection coatings and a highly reflective back contact.

Suppose a semiconductor surrounded by air, through which the incident light passes once and the unabsorbed photons with higher wavelengths transmit from the back of medium, Figure 1-3 (a). By adding an ideal reflector at the bottom of a semiconductor, the propagating light path length becomes twice of semiconductor thickness, Figure 1-3 (b).



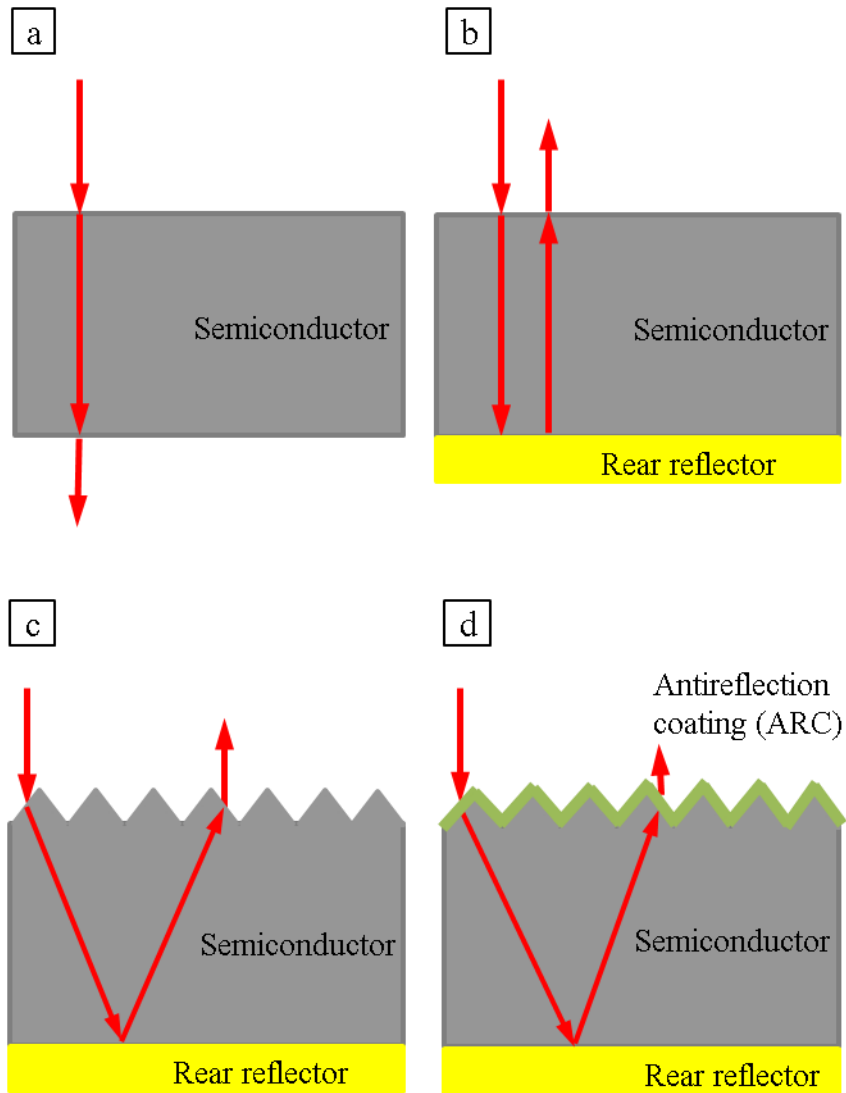


Figure 1-3 shows the incident light path through a bulk semiconductor (a), with a rear side reflector (b), when top surface texturing is added (c), ARCs further reduce the reflectance.

The incident light can be further trapped inside a medium by texturing the top or/and back surface with either random or periodic nanostructures, Figure 1-3 (c). The other approach for light absorption enhancement is to minimize the reflection from the top

surface that can be achieved by gradual change of refractive index, called anti-reflectivity, Figure 1-3 (d).

Thin film solar cell performance can be improved by this approach leading to reduction of the material consumption followed by the cost of green power generation<sup>17,18</sup>.

Light trapping based on ray-tracing is the first approach that is developed in which the theoretical maximum limit of light path length in random surface texturing with period and thicknesses much larger than the sunlight wavelength can be  $4n^2$  where  $n$  is the refractive index of the medium<sup>19</sup>. In more recent works, it is shown that the angle averaged absorption can be enhanced more than ray optics limit in wave optics where there is light interaction with a periodic structure (with period and thickness comparable with the wavelength)<sup>20-22</sup>.

In recent works, a monocrystalline Si wafer is textured by either randomized or periodic structures. An anisotropic alkaline etch, typically KOH results in a random pattern of pyramids since the  $\langle 111 \rangle$  planes etch much slower than the rest of the atomic planes in  $\langle 100 \rangle$  oriented Si wafers<sup>1</sup>. The periodic structures however are fabricated by using photolithography or soft-imprinting lithography<sup>23,24</sup>.

### 1.3.2 Periodic Light Trapping Nano-Structures

A periodic structure, also known as diffraction grating, redirect incident light into discrete directions at certain angles, called diffraction orders, at which the reflected, transmitted and scattered electromagnetic wave superimposed constructively. The diffraction order starts with zero-order where direct transmission or specular reflection

and continues by non-zero integers,  $m$  as illustrated in Figure 1-4. There are variety of works in which periodic structures are applied to the back side<sup>25,26</sup>, front side<sup>27,28</sup> and both sides<sup>29</sup>. These studies include both 1D and 2D periodic structures. Although 1D grating has less complexity in fabrication, 2D grating couples the incident light into more diffraction orders that is in favor of light trapping purpose<sup>21,25</sup>.

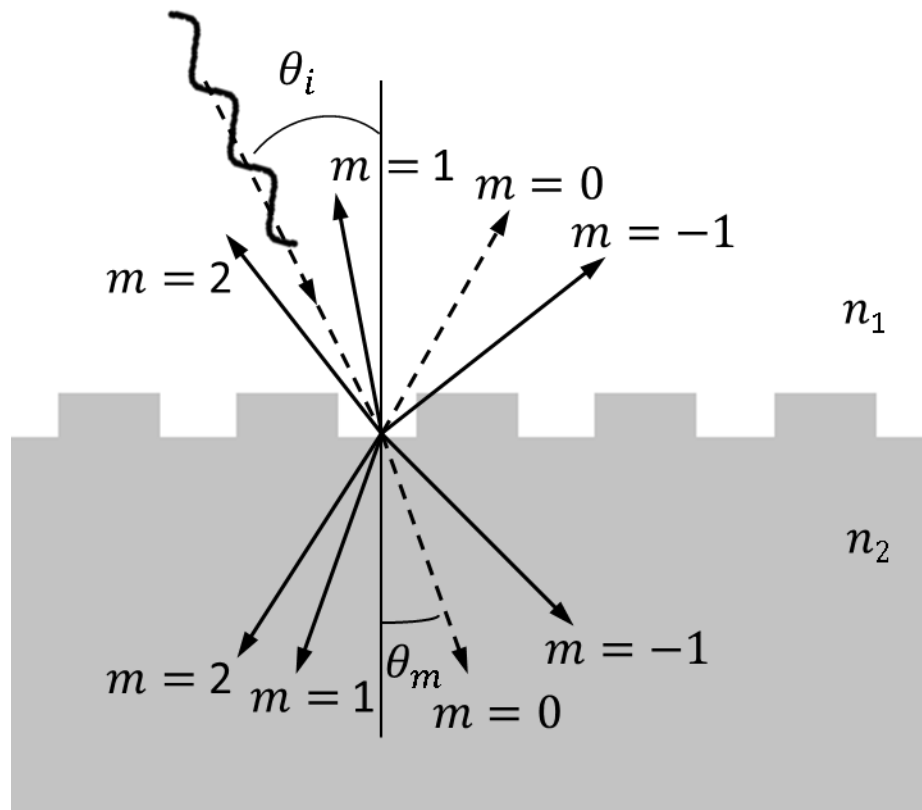


Figure 1-4 shows cross section schematic view of an incident beam creating forward and backward diffraction modes at a 2D periodic grating interface.

The diffraction angles that depend on the refractive index, the period of grating, the wavelength and angle of the incident light for each diffraction order are given by the grating equation<sup>30</sup>

$$n_1 \sin(\theta_i) = \frac{m\lambda}{P} + n_2 \sin(\theta_m) \quad (23)$$

where P is the period of grating,  $n_1$  and  $n_2$  are the refractive indices of the incident and propagating medium,  $\theta_i$  and  $\theta_m$  are the incident and diffraction angles of the  $m^{\text{th}}$ -order respectively. According to this equation at normal incident where  $\theta_i$  is zero,  $P \geq m\lambda/n_2$  has to be satisfied for  $\theta_m = \pi/2$ .

Since the lower diffraction orders have higher intensity, the most efficient way to increase the light path length without losing energy is to redistribute the energy among higher diffraction orders that increases the chance of total internal reflection.

It is found that a periodic structure can increase the light path length beyond the Lambertian limit at normal incident where the absorbing medium thickness or the period of the structure is comparable to the wavelength of light<sup>21,31,32</sup>. However, angular dependency is the limit of periodic structures in comparison with the Lambertian limit.

### 1.3.3 Large Area Nanoscale Patterning

Printing as a promising approach for mass production of thin film solar cell<sup>17,18</sup> has the advantage of producing large scale manufacturing using a roll-by-roll technique. The unique advantage of this process is that a large area master pattern can be fabricated once by using direct laser writing (DLW) technique followed by transferring the pattern

onto a polymeric inverse stamp such as Polydimethylsiloxane (PDMS) that can be used for patterning silicon wafers repeatedly without any degradation as shown in Figure 1-5.

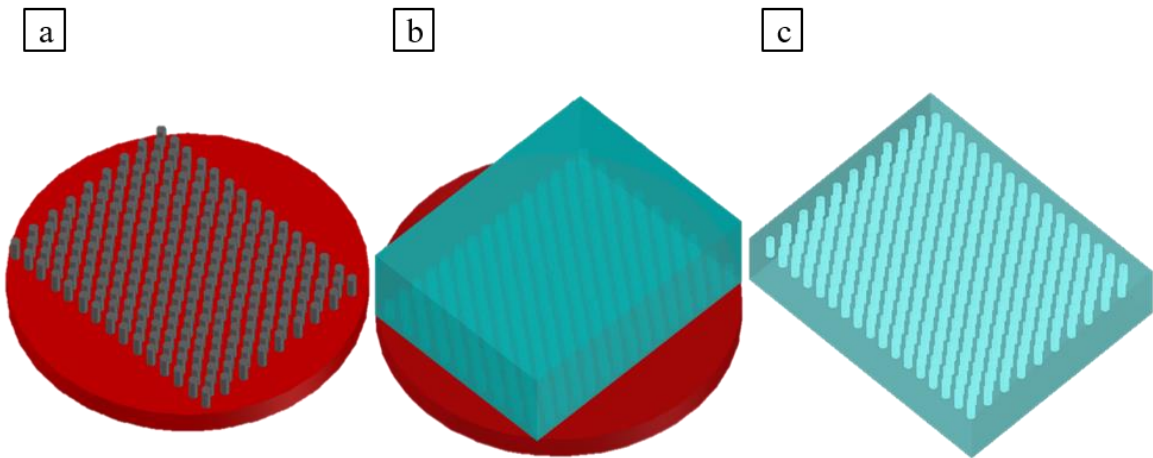


Figure 1-5 (a) shows the fabricated pattern on a master by using DLW technique, (b) then the pattern is transferred onto PDMS mold, (c) that can be used for imprinting repeatedly.

At the end fabricated thin film solar cell is transfer printed on to thin flexible plastic substrate.

#### 1.3.4 Design, Optimization, and Fabrication

In this work, a 2D hexagonal lattice is chosen to maximize the absorption inside the thin film silicon due to the more diffracted beams for the same unit area in comparison with other 2D periodic gratings<sup>33</sup>. Figure 6 shows the 3D FDTD predicted light trapping pattern optimization for a constant silicon thickness (3  $\mu\text{m}$ ). The wavelength integrated absorption is maximized as a function of 2D hexagonal lattice period (P), diameter to

period ratio (D/P) and relief depth (RD) including a constant ARC layer ( $\text{SiO}_2/\text{Si}_3\text{N}_4 = 50/35 \text{ nm}$ ) and 200 nm Au as backside reflector (BSR) for one unit cell area.

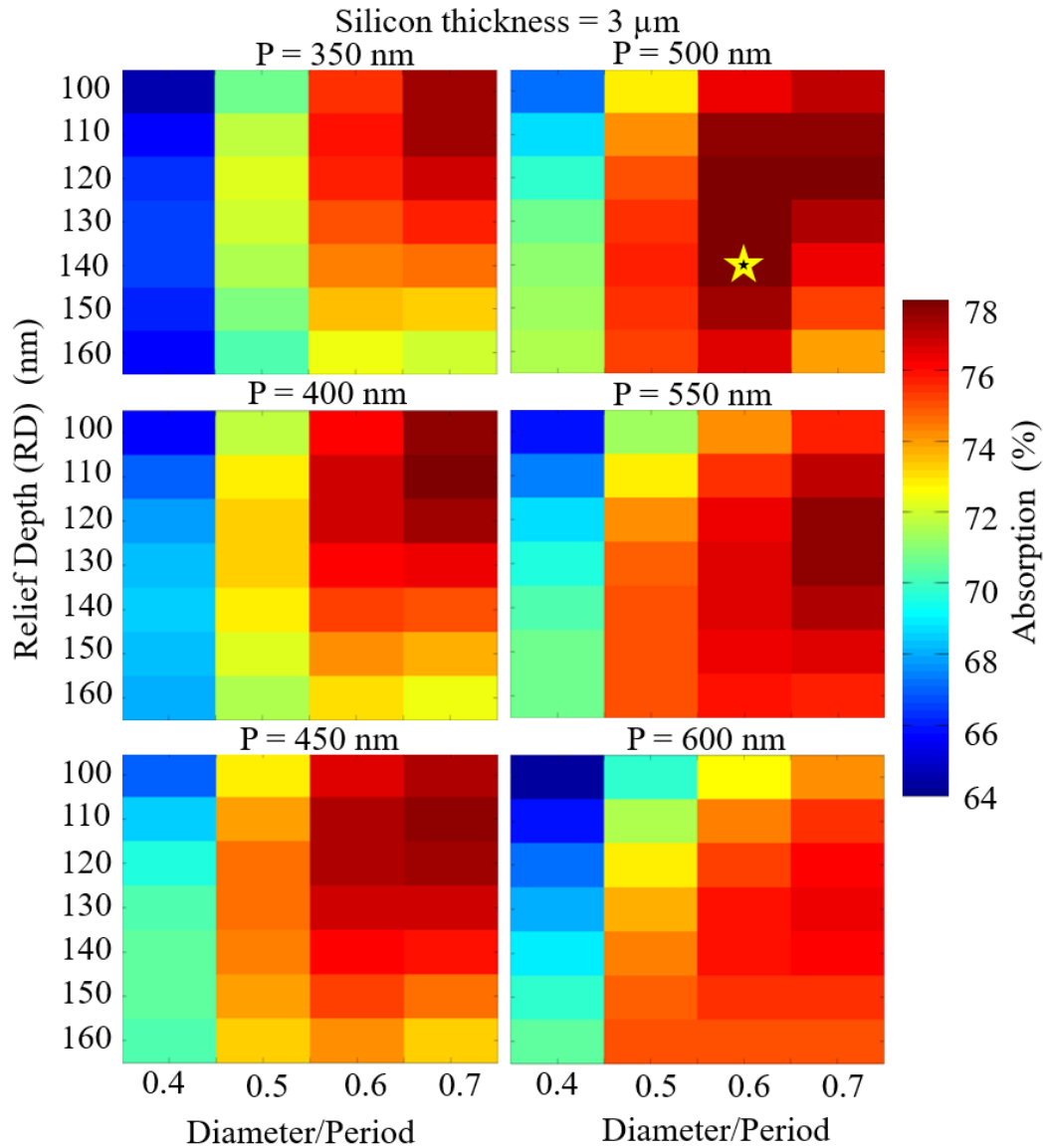


Figure 1-6 FDTD predicted light trapping pattern optimization for a constant silicon thickness ( $3 \mu\text{m}$ ). The wavelength integrated absorption is maximized as a function of 2D hexagonal lattice period, D/P and relief depth ( $P = 500 \text{ nm}$ ,  $D/P = 0.6$ ,  $RD = 140 \text{ nm}$  with ARC ( $\text{SiO}_2/\text{Si}_3\text{N}_4 = 50/35 \text{ nm}$ , chosen from previous work) and 200 nm Au as BSR.

According to Figure 1-6, the optimized light trapping pattern which enables the maximum absorption of 78% integrated solar spectrum (400-1100 nm) (marked as star) defines the posts dimension of period 500 nm, diameter/period 0.6, and relief depth 140 nm. The scanning electron microscopy (SEM) image of the fabricated silicon nano-posts based on the optimized geometry obtained from our modeling results are shown from the top, tilted and side view in Figure 1-7.

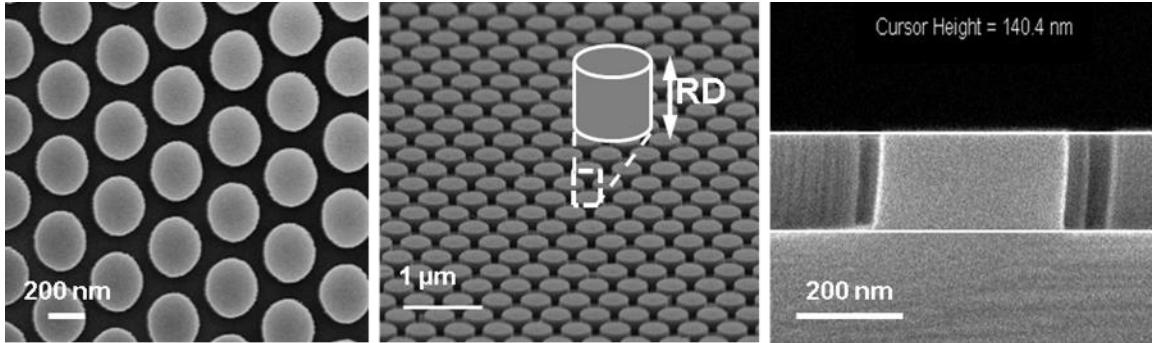


Figure 1-7 (Left to right) top, tilted and cross section view SEM images of fabricated silicon nanostructures as a 2D periodic hexagonal grating.

The process is defining nanoscale light trapping patterns on silicon wafer based on soft nanoimprint lithography. Soft imprinting starts with spin coating  $\sim 500$  nm of a negative photoresist (PR), 5% diluted SU-8 2000.5 is used in this work, on silicon substrate followed by soft baking on a hot plate at  $90$  °C for 1 minute, Figure 1-8 (a). The imprinting takes place afterwards by laminating the PDMS stamp on the sample while it is off and on the hot plate each for 20-30 seconds followed by 1 minute ultra-violet exposure and 1 minute post exposure baking of the sample at  $90$  °C for 1 minute with the purpose of curing and hardening the imprinted pattern on the photoresist, Figure 1-8 (b).

Oxygen plasma de-scum removes PR residues on the unwanted areas, in between the posts, Figure 1-8 (c).

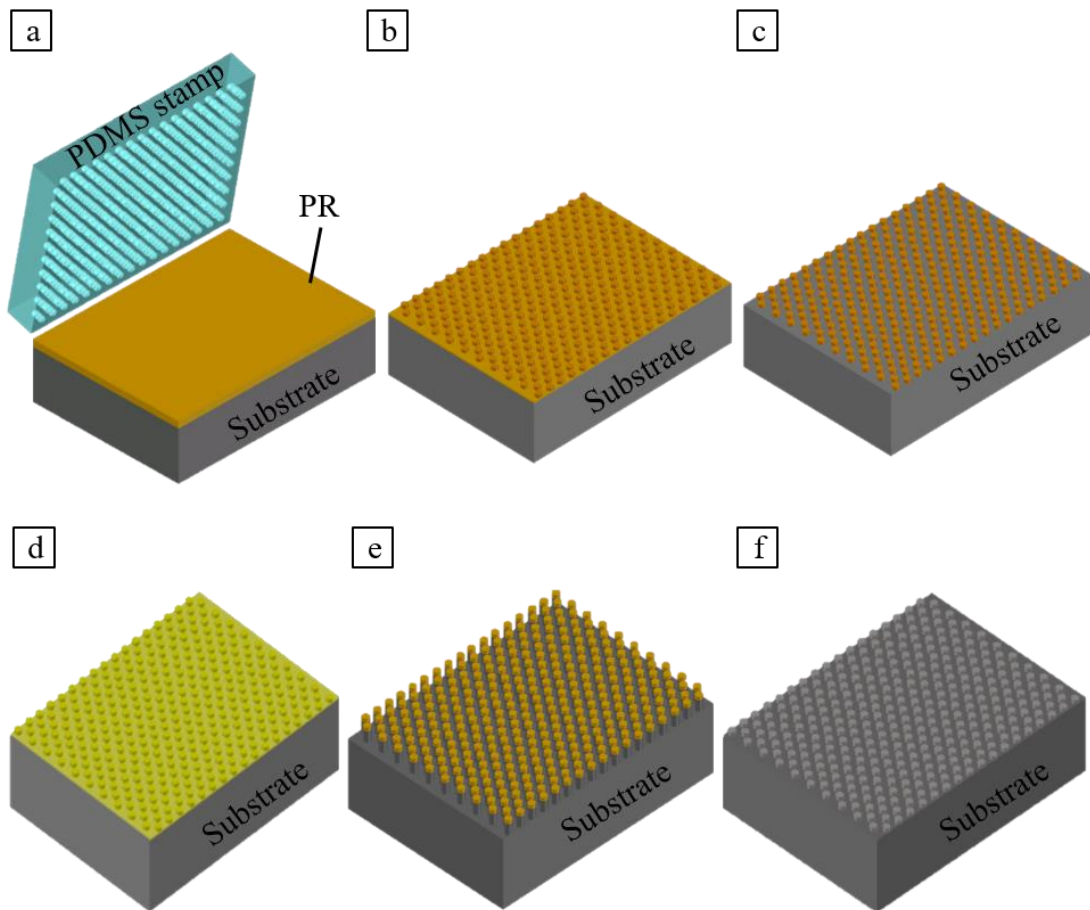


Figure 1-8 (a-c) illustrate the fabrication steps for Soft imprinting from PR spin coating and baking (a), imprinting, UV exposure followed by post exposure baking (b), removing PR residues by  $O_2$  plasma etching (c), to MaCEtch process (d-f) including metal deposition (d), etching silicon in  $H_2O_2:HF:HO_2$  solution (e) and removing the PR (f).

Next step is using the photoresist pillars as a mask to produce the same pattern onto the silicon substrate that can be done by two etching techniques. One etching technique is Reactive Ion Etching (RIE) in which Sulfur Hexafluoride ( $SF_6$ ) with Oxygen ( $O_2$ )



assistant etches silicon where it is exposed to the gas ions. The other technique that is preferred over RIE technique is Metal-assisted Chemical Etching (MaCEtch) which has the advantage of developing well-defined structures and offering more control of the structure geometry and morphology. MaCEtch process starts with a thin layer deposition (both electron beam evaporation and sputtering work) of a noble metal (e.g. Au, Ag, Pt). 35 nm of Au is evaporated in this work, Figure 1-8 (d). The film thickness of 30-50 nm results in neater sidewall characteristics<sup>34</sup>. A mixture of Hydrogen peroxide, Hydrofluoric acid and water ( $\text{H}_2\text{O}_2$ :HF: $\text{HO}_2$ ) with a ratio of 40:10:0.5 ml is used to etch the silicon through the gold interface. At this step, the oxidant injects holes at the metal-semiconductor interface which leads to the oxidation of the semiconductor. The oxidized portion is etched by hydrofluoric acid (HF) in the solution causing the thin metal to effectively “sink” into silicon and creates 3D structure, Figure 1-8 (e). Our process is carried out at room temperature. The gold and SU8 is removed in gold etchant and piranha respectively afterwards, Figure 1-8 (f). There are number of parameters that impact the etch rate and porosity such as silicon resistivity, ratio of the HF to the  $\text{H}_2\text{O}_2$ , metal thickness, temperature, etch time, etc<sup>35</sup>. Figure 9 (a) shows a cross section of well-defined silicon posts that is obtained in our experiments. Etch rate of ( $\text{H}_2\text{O}_2$ :HF: $\text{HO}_2$ ) solution is experimentally obtained for ratios of 40:10:0.5 ml and 40:10:1 ml, Figure 1-9 (b). The result shows that the etch rate doubles by doubling the  $\text{H}_2\text{O}_2$  concentration and increases with time linearly.

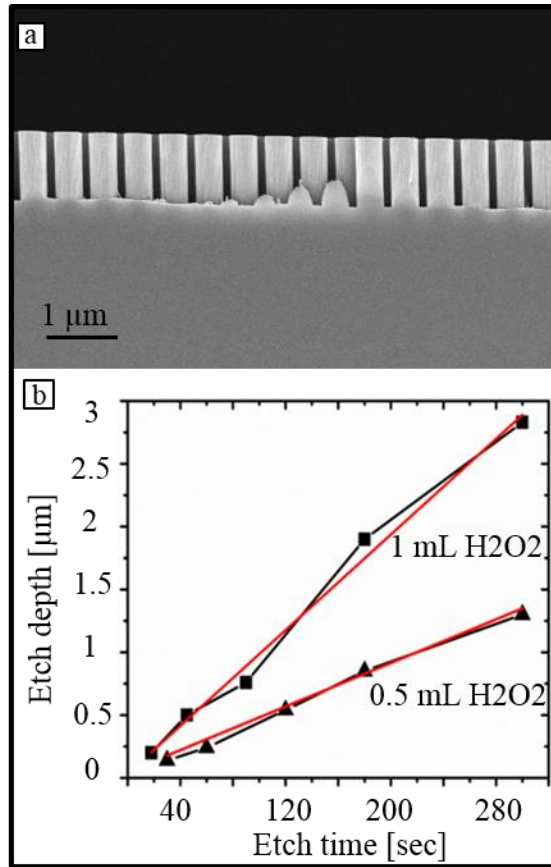


Figure 1-9 (a) shows a SEM image of silicon nanostructures cross section that is etched with MaCEtch technique. (b) shows the experimentally obtained etch rate of silicon at Si/Au interface with 0.5 ml and 1 ml H<sub>2</sub>O<sub>2</sub> concentrations in (H<sub>2</sub>O<sub>2</sub>:HF:HO<sub>2</sub>) solution.

#### 1.4 Dissertation Outline

This dissertation focus is improving the efficiency of thin and ultra-thin c-Si solar cells by advanced light trapping design and implementation in 5 chapters including introduction.

Chapter two presents the design and modeling of an ultra-thin c-Si micro-bar solar cell on which a unified light trapping approach is applied following by a discussion on the fabrication method along with its advantages and limitations. The systematic study,

and optimization of single and double layer anti-reflective coatings on the previously studied top diffractive pattern is the focus of chapter three. The optimized ARC performance over a wide angle range that is important in photovoltaics applications is also discussed in this chapter. Chapter four explains the design, modeling, fabrication and characterization of a 100  $\mu\text{m}$  and 20  $\mu\text{m}$  thin c-Si solar cell followed by analysis of the cell performance. Finally the conclusion of this work is discussed in chapter 5.

## CHAPTER 2      BROADBAND ANGLE INDEPENDENT ANTI-REFLECTION COATINGS ON NANOSTRUCTURED LIGHT TRAPPING SOLAR CELLS

### 2.1    Introduction

The performance of many optoelectronic devices, such as photodetectors and solar cells, rely intrinsically on the efficient absorption of light. Maximizing this absorption, therefore, continues to be of great scientific and commercial interest. Apart from enhancing the absorption within the semiconductor bulk<sup>22,36-44</sup>, there exist many studies on anti-reflective materials<sup>45-48</sup>, their deposition methods<sup>49,50</sup> and nano/micro structured anti-reflection coatings (ARC)<sup>29,51-55</sup> in which they focus on minimizing reflection losses to the amount of light entering the device. Reflection occurs when light passes through the interface of two different mediums with a refractive index mismatch. The most common ARC is a single dielectric layer that serves to bridge the optical impedance of air and the generally high index semiconductor - for a specific wavelength. The ideal ARC meets the effective medium theory (EMT) criteria at which the refractive index gradually increases from the air (ambient medium) to the semiconductor (substrate medium). Although such patterns minimize the integrated reflectivity down to  $<2\%$ <sup>24,54,56</sup>, they do not necessarily maximize the photon absorption in the substrate. For instance, silicon thinner than 200  $\mu\text{m}$  is unable to absorb the full solar spectrum within one optical pass and the unabsorbed light transmits out of the cell - effectively lost. To improve light absorption within thin solar cells, a unified light scattering and anti-reflection scheme is required. Cells structured with two-dimensional diffraction gratings have demonstrated enhanced absorption by increasing the effective path length of light

within the absorbing medium<sup>57</sup>. In our earlier work, we have optimized the wavelength integrated absorption in ultrathin c-Si films (3-6  $\mu\text{m}$ ) structured with a 2D hexagonal array of posts by varying the nanostructure period (P), diameter to period ratio (D/P) and relief depth (RD)<sup>58,59</sup>. While finding the parameters which most effectively scattered light past the air-silicon interface, an optimized ARC could further improve performance by reducing the losses off the nanostructured surface. Here, we perform this optimization and study the impact of conformal antireflection coatings by maximizing absorption averaged over a broad range of wavelengths (400-1100 nm).  $\text{SiO}_2$ ,  $\text{Si}_3\text{N}_4$ , and  $\text{Al}_2\text{O}_3$  films are chosen for this study due to their passivation quality and industrial popularity. Numerical simulations of the single and double layer ARCs are performed using finite difference time domain (FDTD) techniques and serve to guide the fabrication of our experimental solar cells. We employ metal assisted chemical etching (MacEtch) to pattern the light trapping nanostructure into the silicon surface<sup>60</sup>, which serves as a low cost alternative to reactive ion etching (RIE) while maintaining control over structural features and also producing the smooth surfaces needed for quality passivation<sup>61</sup>. We lastly demonstrate the combined, optimized ARC-light trapping system's wide angle independent response needed for high efficiency solar cells.

## 2.2 Results and Discussion

A schematic of the interdigitated back contact c-Si solar cell architecture with a 2D hexagonal top diffractive light trapping pattern is shown in Figure 2-1 (a). The

corresponding top and cross-sectional SEM images of the bare and ARC coated light trapping patterns are shown in Figure 2-1 (b).

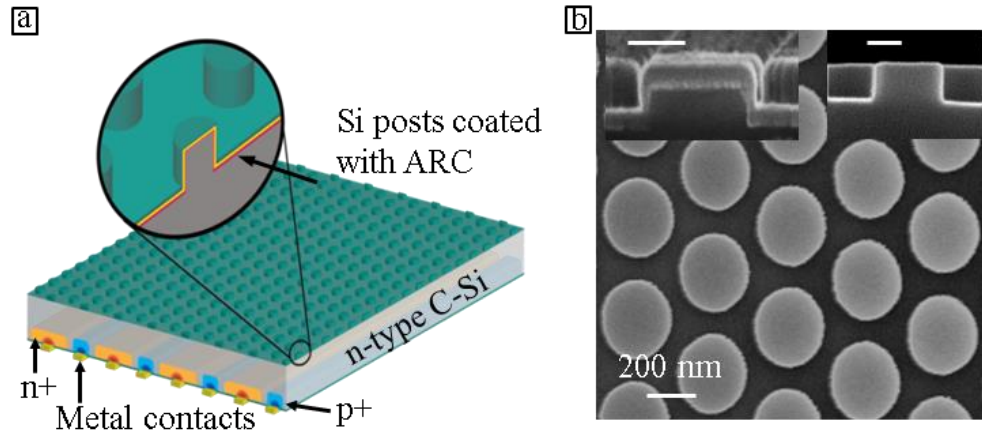


Figure 2-1(a) shows the top and side view SEM images of the bare and ARC coated 2D grating fabricated by using metal assisted chemical etching technique. (b) shows interdigitated back contact solar cell architecture with the light trapping scheme as an application of such angle independent light-trapping nanostructures.

As a guideline for a single layer anti-reflection coating simulations, we begin with reflection from a planar surface that is characterized by the Fresnel equations, and from them derive a condition for destructive interference. This minimum reflectance condition is met when the optical phase length of the ARC is a quarter of the wavelength of light  $n \cdot d = \lambda/4$  ( $d$  is the film thickness) where the refractive index ( $n_{ARC}$ ) must follow<sup>62</sup>  $n_{ARC} = \sqrt{n_{air} \cdot n_s}$ . While potential ARC materials must meet this optical condition, they must also provide a high quality surface passivation to ensure minimal charge carrier loss. Three ARC materials,  $Al_2O_3$ ,  $Si_3N_4$ , and  $SiO_2$ , fit this criterion and are modeled using FDTD simulations on a planar as well as patterned c-silicon substrate. Figure 2-2

(a) shows reflectance as a function of wavelength and thickness of three antireflection coatings on previously reported optimized light trapping pattern<sup>58</sup>. From these simulations, we find a thickness of 80 nm, 50 nm, and 60 nm are needed for single layer of  $\text{SiO}_2$  ( $n = 1.47$ ),  $\text{Si}_3\text{N}_4$  ( $n = 2$ ), and  $\text{Al}_2\text{O}_3$  ( $n = 1.67$ ), respectively. These values correspond to wavelength-integrated reflectance values of 3.4% for  $\text{SiO}_2$  and 3.2% for  $\text{Si}_3\text{N}_4$  and  $\text{Al}_2\text{O}_3$  on the patterned silicon as indicated by white dash lines in Figure 2-2 (a).

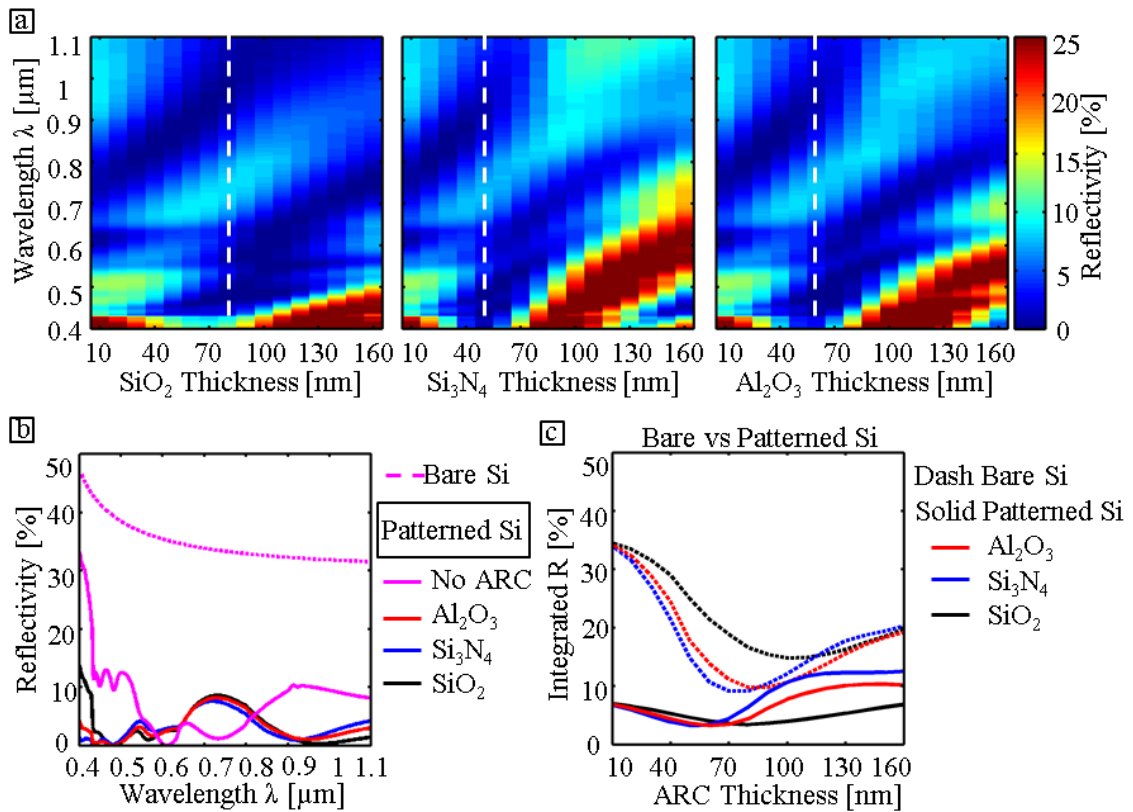


Figure 2-2 (a) reflectance as a function of wavelength and thickness for three single layer ARCs for nanostructure period 500 nm, relief depth 140 nm and diameter 320 nm. White lines indicate the thickness that gives the minimum reflectance. (b) compares the reflectance vs wavelength of bare silicon (magenta dash line), patterned silicon

(magenta), and patterned Si coated with Al<sub>2</sub>O<sub>3</sub> (red), SiO<sub>2</sub> (black) and Si<sub>3</sub>N<sub>4</sub> (blue) conformal with the thicknesses indicated with white dash lines in (a). (c) compares the wavelength integrated reflectance as a function of ARC thicknesses for bare (dash) and patterned silicon (solid).

These optimum, wavelength-dependent minimum reflections are plotted in Figure 2-2 (b) alongside the reflection from bare, patterned silicon substrates without ARCs for comparison. From this plot, we show that the light trapping pattern alone reduces reflection significantly over the visible spectral range from average 34.6% to 8.1%. However, in the near-IR wavelength range (0.8-1.1  $\mu\text{m}$ ), the light trapping pattern incurs high reflection loss (>10%) which is much larger than that of the ARC coated light trapping pattern (<3.5%). According to the results in Figure 2-2 (b) the wavelengths at which there is a dip in the patterned Si reflectance spectrum are different from the ones in the ARC coated patterned Si.

While certain applications may require optimization of reflectance at specific wavelengths, solar cell ARCs should be considered over a wide range of wavelength (400 nm – 1100 nm). As such, Figure 2-2 (c) shows the wavelength-integrated reflectance over a wide range of thicknesses for all three ARC on bare and patterned silicon. According to this figure, the minimum reflection from a single layer SiO<sub>2</sub>, Si<sub>3</sub>N<sub>4</sub>, and Al<sub>2</sub>O<sub>3</sub> on patterned silicon is obtained at 100 nm, 70 nm, and 80 nm, respectively, which correspond to reflectance reduction enhancements of 65%, 67%, and 77% with respect to the minimum reflectance obtained from the bare silicon with ARC.

In the above numerical studies, all ARC coatings are considered to be conformal (i.e. having a uniform thickness across the nanostructured surface). However, in reality,



there are a number of factors which impact the uniformity of ARCs such as deposition methods (PECVD, LPCVD, ALD, etc.), temperature, gas environment, deposition rate, and the underlying structure dimensions and aspect ratio<sup>63</sup>. Step coverage is defined by the ratio of a deposited film thickness on the sidewall of a step over the thickness on the top/bottom surface as shown in the schematic of Figure 2-3 (a).

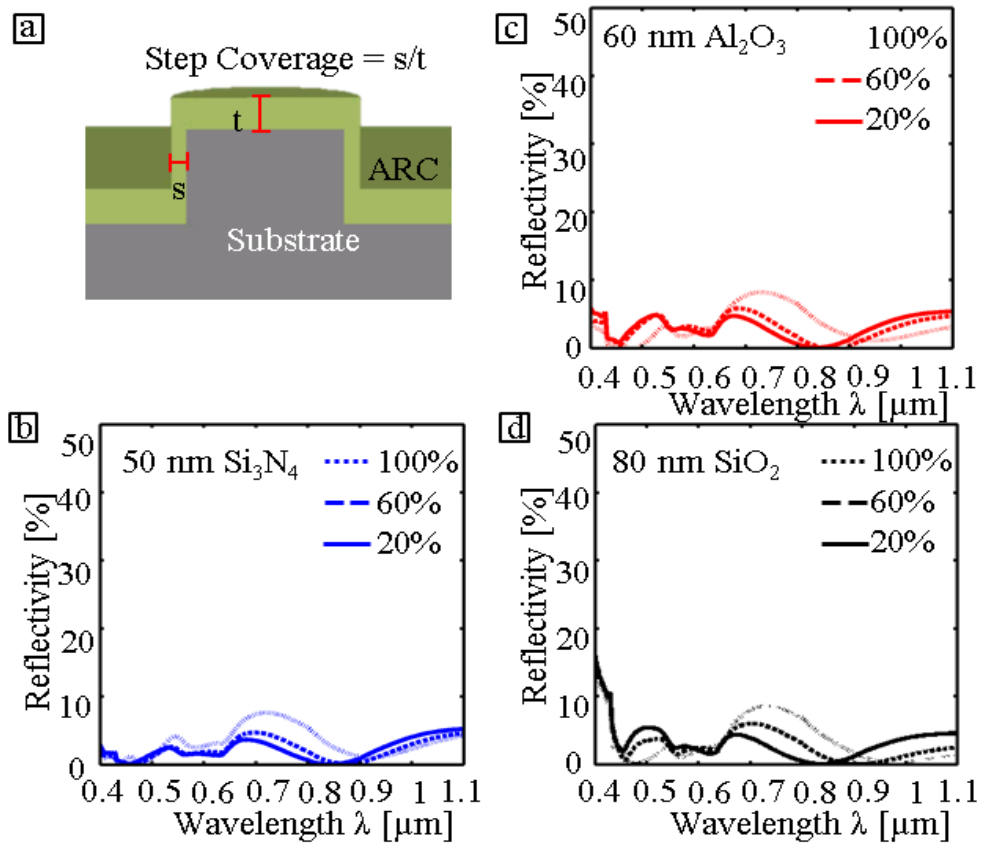


Figure 2-3 (a) schematic of step coverage of a silicon post coated with single layer ARC. (b-d) A comparison of reflectance vs wavelength of  $\text{Al}_2\text{O}_3$  (a),  $\text{Si}_3\text{N}_4$  (b), and  $\text{SiO}_2$  (c) coatings with 20%, 60%, and 100% step coverages.

To investigate the impact of step coverage on the reflectivity, and therefore performance of the anti-reflective material, we performed numerical simulations and compared them to experimental data. Reflectance vs wavelength data is obtained for all three ARC at their optimum thicknesses for three different step coverage values from conformal (100%) to 20%, Figure 2-3 (b-d). Interestingly, we observe a blue shift in the reflectance spectrum along with a reduction in reflection for ARCs with lower step coverage. From experiment, we find step coverage values for PECVD SiO<sub>2</sub> and Si<sub>3</sub>N<sub>4</sub> at 300°C and Atomic Layer Deposition (ALD) Al<sub>2</sub>O<sub>3</sub> at 200°C of 20%, 60%, and 80%, respectively.

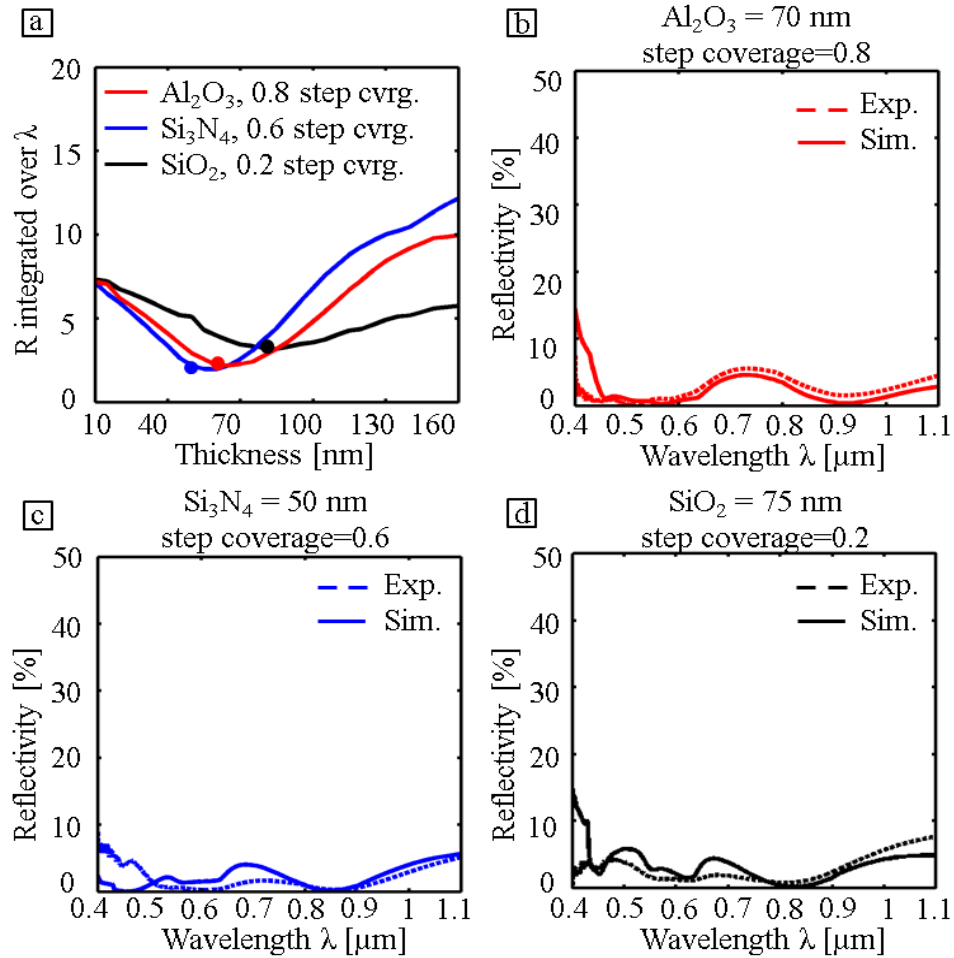


Figure 2-4 (a) reflectance over a broadband wavelength regime (400- 1100 nm) for three single layer non-conformal antireflection coatings. The dots indicate the thicknesses at which the measured reflectance spectra is matched with the equivalent predicted one for Al<sub>2</sub>O<sub>3</sub> (b), Si<sub>3</sub>N<sub>4</sub> (c), and SiO<sub>2</sub> (d).

Using these values, we simulate the integrated reflectance as a function of thickness and obtain their respective optimal ARC thicknesses (shown in Figure 2-4 (a)). Dots in the respective plot correspond to experimental data points. Figure 2-4 (b, d) shows the experimental measurements for these optimized ARCs and a close correspondence between numerical predictions. We believe the minor mismatch between

experiment and numerical results are due to slight differences in refractive index and nanostructure dimensions between the deposited film and the index used in the modeling.

Another implication of the Fresnel equations is that a gradual change in refractive index will result in a lower reflection between two media. To implement this and further reduce reflection loss, we now consider a bi-layer ARC. The conditions which minimize reflection for a planar double layer ARC is given by<sup>62</sup>,  $n_1 d_1 = n_2 d_2 = \lambda/4$ , where  $n_1/n_2 = \sqrt{n_{air}/n_s}$ . For a Si<sub>3</sub>N<sub>4</sub> and SiO<sub>2</sub> bi-layer, this corresponds to a thickness of 70 nm and 90 nm, respectively. Both silicon nitride and silicon oxide can be deposited in a Plasma Enhanced Chemical Vapor Deposition system (PECVD) at the same temperature (300 C) which keeps the fabrication process cost effective. We then perform a two-dimensional parameter sweep about these thicknesses (10 nm - 150 nm) to predict the optimum thickness of each layer for the bi-layer ARC on the light trapping structure. According to the result of our simulations, the numerically predicted integrated reflectance gives a minimum reflectance of 2.4% at 20 nm Si<sub>3</sub>N<sub>4</sub> and 70 nm SiO<sub>2</sub>. In the non-conformal case, corresponding to our experimental fabrication (60% Si<sub>3</sub>N<sub>4</sub>- 20% SiO<sub>2</sub>), the minimum integrated reflectance of ~1.5% is obtained at a range of 60 nm Si<sub>3</sub>N<sub>4</sub>, 100-130 nm SiO<sub>2</sub> and 70 nm Si<sub>3</sub>N<sub>4</sub>, 100-120 nm SiO<sub>2</sub> over a broadband wavelength regime (400-1100 nm), Figure 2-5 (a). The lower reflectance value of the non-conformal simulation is due to the better performance of lower step coverages on the top diffractive pattern that was shown in Figure 2-3. In order to verify this result, the reflectance vs wavelength of a patterned silicon coated with a chosen thickness of 70 nm

$\text{Si}_3\text{N}_4$  and 100 nm  $\text{SiO}_2$  (60%  $\text{Si}_3\text{N}_4$ - 20%  $\text{SiO}_2$ ) is measured. Figure 2-5 (b), confirms that there is a fair agreement between simulation and experimental results.

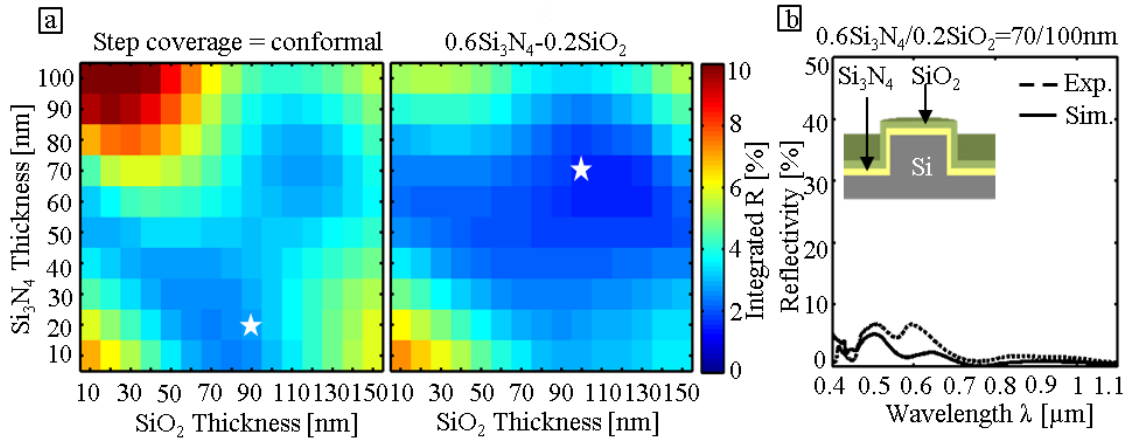


Figure 2-5 (a) shows predicted wavelength integrated reflectance as a function of  $\text{Si}_3\text{N}_4$ - $\text{SiO}_2$  bilayer ARC thickness for conformal and non-conformal coatings on patterned silicon. The optimum ARC thicknesses at which the minimum reflection is obtained are marked as star. (b) presents experimentally measured and predicted reflectance vs wavelength for non-conformal 70 nm  $\text{Si}_3\text{N}_4$ - 100 nm  $\text{SiO}_2$  bilayer coatings are in a good agreement.

Finally, to quantify how these ARCs will perform in the field, where incident light will strike the surface at a wide range of angles throughout the day, we investigate the combined wavelength and angular response of the system. The predicted reflectivity integrated over wavelength of the bilayer ARC as a function of incident angle is shown in Figure 15 that remains below 3% from  $0^\circ$ - $60^\circ$  over the visible regime (400-850nm). Not only is the double layer ARC performance better than a single layer ARC in terms of low reflectivity, but its overall angle dependency is 53% lower than its individual components at their optimum thicknesses. We experimentally verify these simulations in Figure 2-6

by using an integrating sphere to obtain the angle and wavelength resolved reflectance spectra<sup>64</sup>.

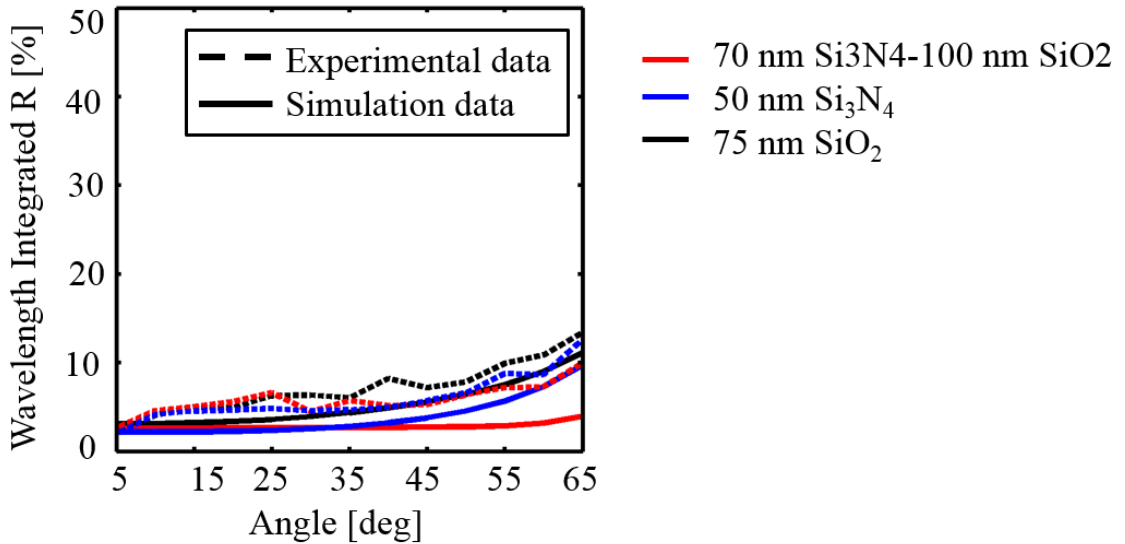


Figure 2-6 compares predicted and experimentally measured angle resolved reflectance from the optimized ARC coated patterned silicon.

For practical limitations such as beam and sample size, the angle is scanned between 5 degrees and 65 degrees. Unpolarized light is used for the angle resolved measurements and to obtain the equivalent through simulation, we average the s-polarized and p-polarized simulation results for a given angle by using the broadband fixed angle source technique (BFAST) from Lumerical FDTD. The measured angle resolved integrated reflectance for the optimized bi-layer ARC coated patterned surface shows a better performance in comparison with the single layer ARCs and remain below 5% up to 45° and below 10% up to 65° over the silicon absorption band. The consistency between the simulation and experiment for the bi-layer ARC is less than the single layer

ARCs due to the increased sensitivity of the bi-layer reflectance to differences in experimental and numerical refractive indices.

## 2.3 Methods

### 2.3.1 Fabrication

Per previous study<sup>58</sup>, the optimized geometry is obtained with 500 nm period, 300 nm post diameter and 140 nm relief depth. In this work, we used metal-assisted chemical etching (MacEtch) technique to develop the top diffractive hexagonal cylindrical posts that is described in chapter 1. Anti-reflection coating (ARC) deposition is done using atomic layer deposition (ALD) with a Savannah 2 system for aluminum oxide at 200 °C with 0.04 sec water and 0.1 Trimethylaluminum (TMA) pulse time, 80 sccm carrier gas flow, 200 mTorr pressure. Silicon nitride deposition is done using a Plasma-Therm 790 plasma enhanced chemical vapor deposition (PECVD) system at 300 °C. 2% Silane gas diluted in Nitrogen (N<sub>2</sub>) is used with the following gas flows: 120 sccm SiH<sub>4</sub>, 4.56 sccm NH<sub>3</sub>, 400 sccm N<sub>2</sub>, 900 mTorr pressure, 20 W RF power with deposition rate of 8-10 nm/min. Silicon oxide is also deposited using the same system at the same temperature with 200 sccm SiH<sub>4</sub>, 412 sccm N<sub>2</sub>O, 1050 mTorr pressure, 25 W RF power and deposition rate of 48-50 nm/min.

### 2.3.2 Optical Measurements and Imaging

Normal angle reflection spectra is measured using a Fourier transform infrared (FTIR) spectrometer Vertex 80 system with a CaF<sub>2</sub> UV-VIS-NIR beam splitter, silicon

diode detector that is coupled to a 4x objective 0.07 numerical aperture mounted on an optical microscope Hyperion 1000 system. An aluminum mirror is used as the background reference. Angle resolved reflectance spectra are collected using RTC-060-SF Reflectance/Transmittance integrating sphere coupled to a KI-120 Koehler collimated illuminator in the VIS-NIR region (LabSphere).

### 2.3.3 Modeling

Reflection spectra are numerically calculated with Finite-Difference Time-Domain (FDTD) software package (Lumerical Solutions Inc) based on the experimental parameters for the imprinted 2D grating structure and the ARC layers. The wavelength dependent refractive index of silicon oxide and aluminum oxide are taken from Palik and silicon nitride from Phillip.

## 2.4 Conclusion

In this chapter, we have optimized the design of a broadband, angle independent anti-reflection coating for use on nanostructured solar cells. The reflectivity behavior of three single layer and a bilayer anti-reflection coatings on patterned and bare silicon is predicted and experimentally measured for conformal and non-conformal coatings. Simulation shows that lower step coverage of a deposited film results in a lower wavelength integrated reflectance. To further reduce the reflectance from the top nanostructured surface, a double layer ARC is modeled. The integrated reflectance from an optimized non-conformal single layer  $\text{SiO}_2$ ,  $\text{Si}_3\text{N}_4$ , and  $\text{Al}_2\text{O}_3$  is predicted to be 3%, 2.2%, and 2.3% respectively whereas 1.5% from a bi-layer ARC,  $\text{Si}_3\text{N}_4$ -  $\text{SiO}_2$ , both of



which are very low over a wide range of wavelengths compared to other ARC structures. The experimental results of the reflectance vs wavelength that are plotted next to the predicted result are fairly in agreement with the simulations. Lastly, we have shown that the optimized bi-layer ARC is significantly independent of the angle of incident with <4% wavelength integrated reflectance up to the angle of  $60^\circ$  which makes it very promising for photovoltaic applications.

## CHAPTER 3 UNIFIED ELECTROMAGNETIC-ELECTRONIC DEVICE DESIGN

### 3.1 Introduction

Low cost and high efficiency solar cells are an important alternative to fossil fuel based energy. Mono-crystalline silicon (c-Si) is undoubtedly the material of choice in photovoltaic applications due to its high natural abundance, low cost, reliability, excellent optical/electronic properties and chemical/radiation hardness<sup>1,14,65,66</sup>. However, there is a continued demand for thinner, lighter and more efficient solar cells. Present commercial screen-printed c-Si cells are typically 150-180  $\mu\text{m}$  thick, enabling large absorption of the solar spectrum over the silicon bandwidth, and obtain 17-20% energy conversion efficiency in volume production<sup>3,4,65</sup>. While reducing the thickness of c-Si can decrease the absorption significantly for thickness below  $\sim 50 \mu\text{m}$ , it has been shown that it leads to a higher voltage<sup>67-69</sup> with the added benefit of reduced material costs<sup>53,70,71</sup>. As the cell thickness decreases, the diode saturation current decreases, resulting in the increase in voltage. In order to compensate for the low absorption of ultra-thin ( $< 30 \mu\text{m}$ ) c-Si cells, special light management schemes were developed<sup>29,36,37,72,73</sup>. Various light trapping schemes were proposed and demonstrated in recent years to enhance absorption in thin-film geometry based on top and/or bottom diffractive/plasmonic light scattering patterns<sup>22,41,44,64,74-78</sup>. In previous works light trapping in ultra-thin silicon solar cells have been shown and significant enhancement in energy conversion efficiency in a functional cell has been demonstrated for the first time<sup>79,80</sup>. However, light trapping solar cells must also ensure maximum charge carrier collection in order to fully benefit from the increase

in photon absorption. Maximizing photon absorption without efficient electron collection is not adequate to obtain higher efficiency. An electronic device physics model which includes light trapping within functional cell geometries is missing from the present literature. Thus, there is a need for a unified photon-electron harvesting scheme that enables the design of high efficiency, functional, commercial grade solar cells. This will translate to enormous material cost savings (greater W/g silicon utilization) and provide other mechanical attributes such as light-weight and flexibility to the resultant solar modules. Here, we report a unified electromagnetic and electronic device physics design approach which maximizes the combined photon-electron harvesting. The spatial absorption profile of the light trapping solar cell predicted from finite difference time domain (FDTD) simulations define the charge carrier generation in the following electronic device simulation. The predicted short circuit current ( $J_{sc}$ ), open circuit voltage ( $V_{oc}$ ) and efficiency ( $\eta$ ) from an optimized doping profile and carrier life time closely match experimental observations in bare as well as light trapping cell geometries.

## 3.2 Results and Discussion

### 3.2.1 Light Trapping c-Si Solar Cell Optical Responses

Figure 3-1 shows the chosen light trapping cell architecture. The light trapping scheme is composed of top nanostructured diffractive optical element coated with anti-reflection coating coupled to an optical cavity which enhances absorption via a composite phenomenon: reduction in reflection, path length enhancement via forward diffraction and trapping light into the silicon waveguide and cavity modes.

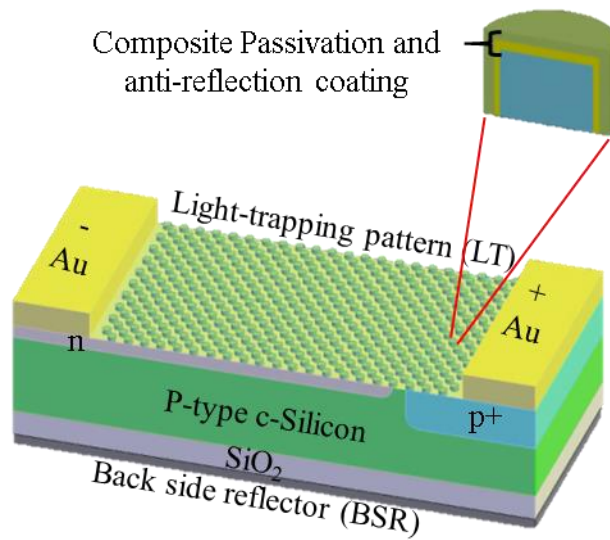


Figure 3-1 illustrates the c-Si solar cell architecture which combines the light trapping scheme with the functional cell geometry.

An integrated 78% absorption with respect to the AM1.5G spectrum is numerically predicted inside the 3  $\mu\text{m}$  thick light trapping cell as shown in Figure 3-2.

This constitutes 117% absorption enhancement compared to a bare wafer of same thickness which absorbs only 36% of the integrated solar spectrum. For the top diffractive pattern a 2D hexagonal Bravais lattice was chosen based on the design reported in our earlier publications<sup>27, 39</sup>.

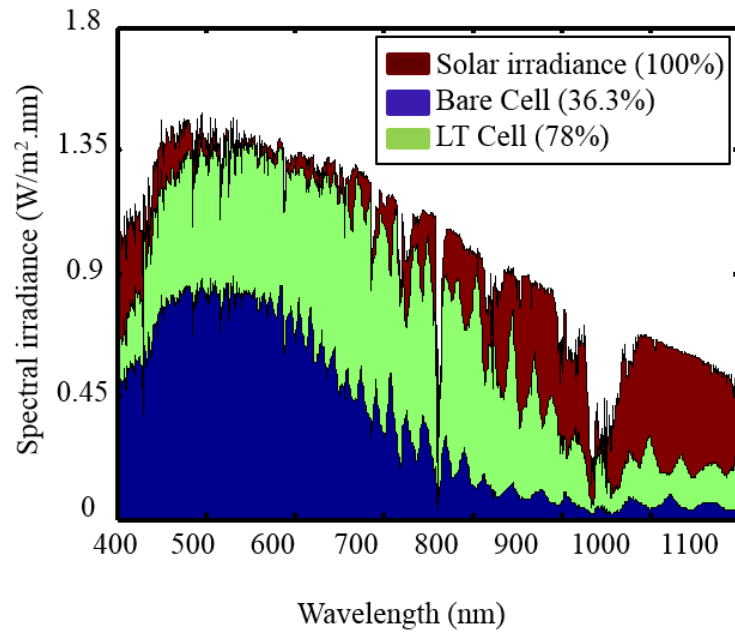


Figure 3-2 shows the absorbed photo flux as a function of wavelength with reference to AM1.5D solar spectrum for bare and light trapping cell inside a 3  $\mu\text{m}$  thick wafer.

Figure 3-3 presents the band diagram of the corresponding n-p-p+ junction under illumination when is connected to an external load.

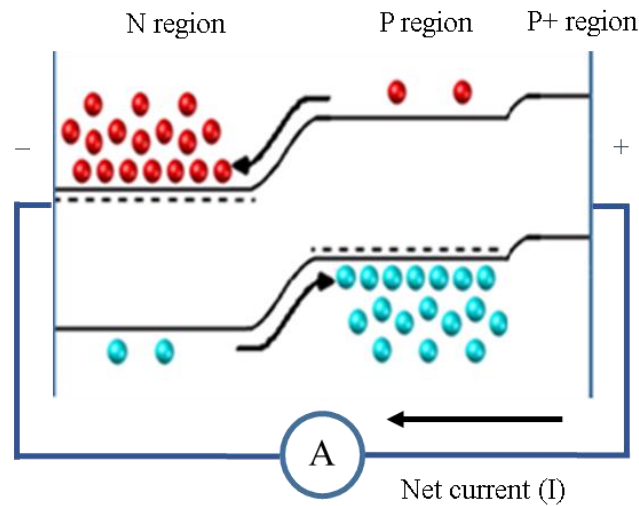


Figure 3-3 shows the corresponding band diagram under illumination.

The lack of the acceptor impurity concentration at the base contact causes the minority carriers to recombine more easily, which is considered one of the main sources of the voltage loss in a solar cell<sup>44</sup>.

Hence, a heavily p-doped region at the base electrode improves the open circuit voltage. The band tilts downwards in the n region and upwards in the p region due to the positive and negative charge movement, respectively. Under illumination, the number of generated excess electrons is equivalent to the number of generated excess holes; hence the Fermi energy difference at the n and p sides,  $\epsilon_{fn} - \epsilon_{fp}$  becomes closer to the band gap energy by increasing the numbers of excess minority carriers which leads to higher current density. This phenomenon is further described in the following section.

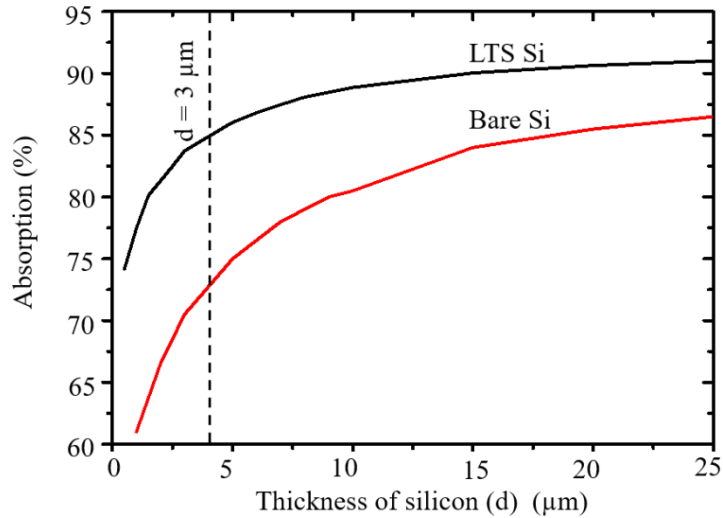


Figure 3-4 shows silicon absorption as a function of silicon thickness for the optimized light trapping pattern ( $P = 500$  nm,  $D/P = 0.6$ ,  $RD = 140$  nm with ARC ( $\text{SiO}_2/\text{SiN} = 50/35$  nm), and 200 nm Au as BSR) vs bared silicon.

Based on the optimized pattern, the silicon absorption as a function of silicon thickness is studied and shown in Figure 3-4. It can be seen that for this light trapping design silicon thickness of  $> 15$   $\mu\text{m}$  is needed in order to absorb  $> 90\%$  integrated AM1.5 solar spectrum. Figure 3-5 compares the FDTD predicted absolute absorption of a 3  $\mu\text{m}$  thick bare and a light trapping cell as a function of wavelength. Significant absorption enhancement can be observed in the light trapping cell especially near the band edge where bare silicon absorption is weak. Furthermore, narrow Fabry-Perot cavity resonances are observed in the light trapping cell which correspond to the presence of the  $0^{\text{th}}$  and higher order cavity modes of the thin cell.

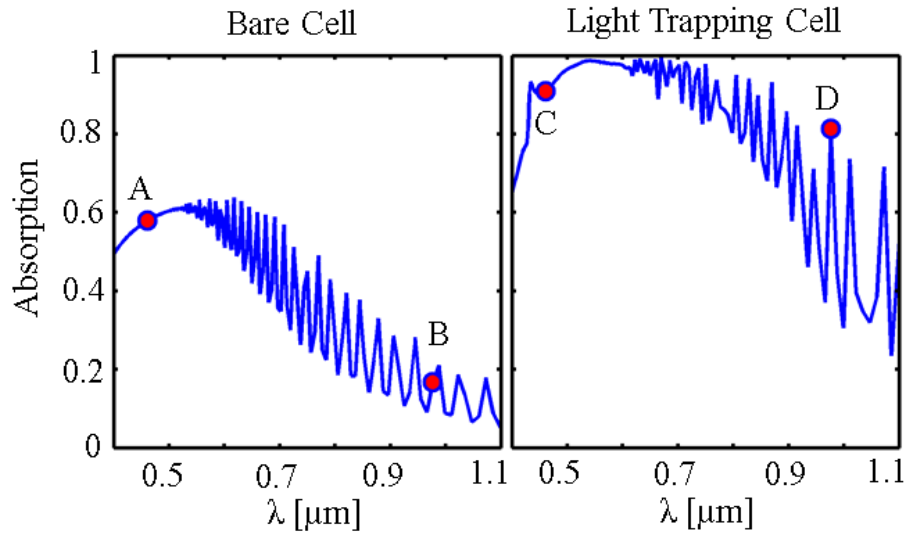


Figure 3-5 compares the FDTD predicted absolute absorption inside 3  $\mu\text{m}$  thick bare and light trapping cells.

The FDTD predicted 2D absorption profiles ( $P_{\text{abs}}$ ) of bare and light trapping cells in a strong ( $\lambda = 461 \text{ nm}$ ) and weak ( $\lambda = 977 \text{ nm}$ ) absorption regimes are shown in Figure 3-6.

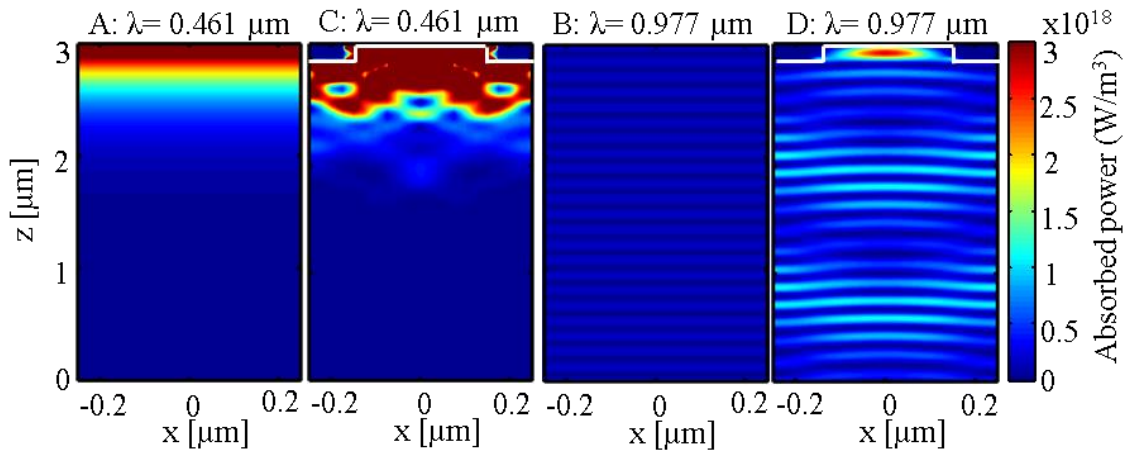


Figure 3-6 illustrates the power absorbed per unit volume in 3  $\mu\text{m}$  thick bare and light trapping cell at strong ( $\lambda = 461 \text{ nm}$ ) and weak ( $\lambda = 977 \text{ nm}$ ) absorbing regimes.



Absorbed power is obtained by applying Equation (26), which is derived from the divergence of the Poynting vector formula as

$$P_{abs} = -\frac{1}{2}\omega|E|^2 \text{Im}(\epsilon) \quad (24)$$

According to the Equation (26), the energy absorption of a monochromatic light is directly proportional to the electric field intensity which mandates field enhancement for higher absorption. As predicted, the band edge photons ( $\lambda = 977$  nm) are more strongly absorbed in the light trapping cell compared to the bare cell due to tight field confinement and path length enhancement via diffraction/scattering. There is significant enhancement in absorbed power between light trapping and bare cells which can be noticed by comparing Figure 3-6, left and right.

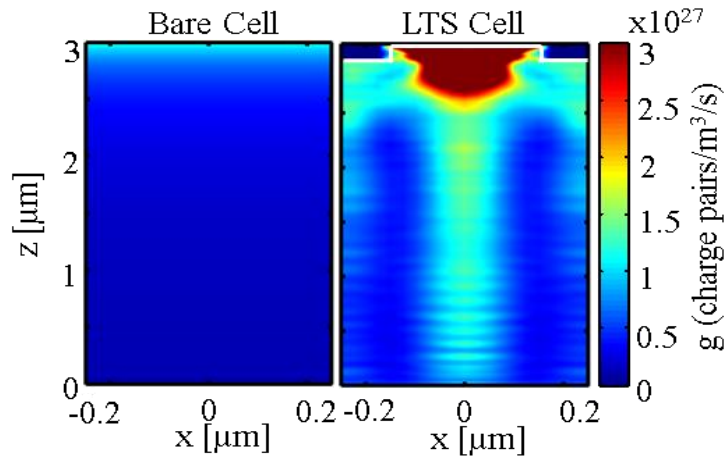


Figure 3-7 compares the wavelength integrated charge carrier generation rate ( $g$ ) over a 2D plane across the center of the hexagonal unit cell.

This fact is further supported by the wavelength integrated generation rate ( $g$ ) in Figure 3-7. The number of electron-hole pairs generated by absorbed photons as a function of position integrated over a specific wavelength range in the device is defined as the wavelength integrated charge carrier generation rate ( $g$ ). From Figure 3-7, significantly enhanced charge carrier generation can be observed for the light trapping cell due to the stronger photon absorption substantially deep inside the wafer. Subsequently, the FDTD predicted 3D generation rate data is imported into the numerical electronic modeling (Lumerical DEVICE, Lumerical Inc.) that makes the bridge between electromagnetic absorption and electronic device performance predictions. Since the actual cell is longer than one unit cell due to the lateral p-n junction (Figure 3-1), the FDTD predicted one unit cell generation rate, which is calculated with the periodic boundary condition along the x-y directions, is copied along the length of the device to cover the distance between two contacts.

### 3.2.2 Electronic Device Modeling

The quasi fermi energy levels, electron-hole densities and recombination losses of the cell were extracted from the electronic simulations in order to understand the fundamental gain and loss mechanisms. For a fair comparison, both bare and light trapping cells are assumed to be perfectly passivated with reasonably low surface recombination velocity (SRV)  $SRV = 10$  m/cm. A low SRV isolates the effects of recombination and electron-hole generation processes.

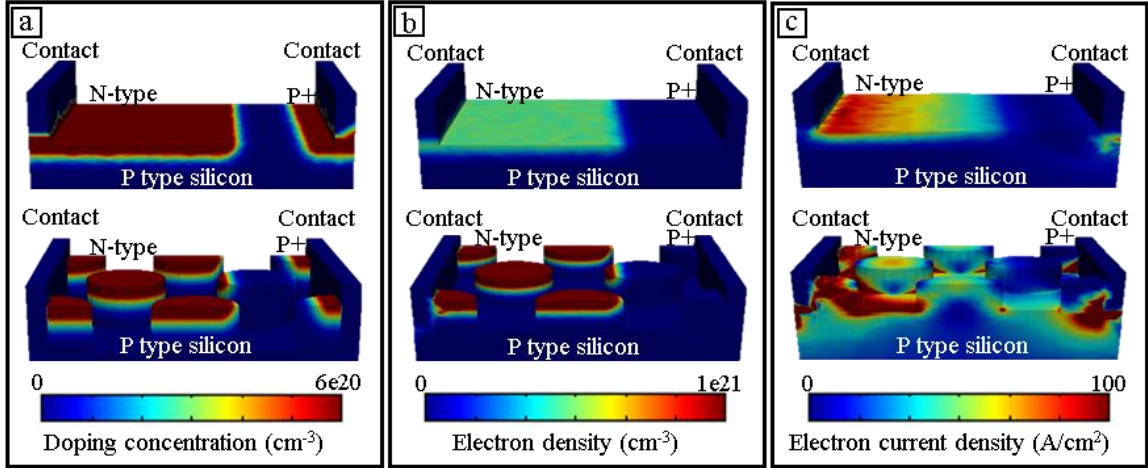


Figure 3-8 (a) shows the doping profile of the 3  $\mu\text{m}$  thick silicon cell with and without light trapping. The p and n regions are defined which show the gradient of impurities in the device. (b) compares the electron density of a 3  $\mu\text{m}$  bare cell with light trapping cell. The electron density in n-type region of the light trapping cell is higher than that of the bare cell, and (c) shows the corresponding electron current density. The structure geometries in this figure are not to scale. The color bar upper and lower limits are chosen in order to enhance the contrast.

Figure 3-8 (a) shows the chosen doping profile of the 3  $\mu\text{m}$  silicon cell with and without light trapping. The p and n regions are shown as gradient of the doping concentration using two opposite color schemes. Figure 3-8 (b) compares the electron density of a 3  $\mu\text{m}$  bare and light trapping cells. The light trapping cell shows a higher absolute electron (and hole) density due to the higher absolute quasi fermi energy levels which, in turn, originates from the higher absorption. The electron density in non-equilibrium conditions (i.e. under illumination as a function of the quasi fermi energy) is given by

$$n = N_C \exp\left(\frac{\epsilon_{fn} - \epsilon_c}{k_B T}\right) \quad (25)$$

where  $N_C$  is the effective density of state in the conduction band,  $\epsilon_{fn}$ , and  $\epsilon_c$  are electron quasi fermi energy and conduction band energy respectively. The carrier density is highly sensitive to any small variation in quasi fermi energy level. As can be seen in Figure 3-8 (b), the electron density within the n-type region of the light trapping cell is significantly higher than that of the bare cell. The n and p quasi fermi energy difference ( $\epsilon_{fn} - \epsilon_{fp}$ ) is a measure of the deviation from equilibrium. Under non-equilibrium conditions, i.e. under illumination, the current density can be written as

$$J_n = \mu_n n \frac{d\epsilon_{fn}}{dx} \quad (26)$$

where  $\mu_n$  is the electron mobility. The electron density in the non-equilibrium condition is  $n = n_0 + \Delta n$  where  $n_0$  is the donor impurity concentration (at equilibrium) and  $\Delta n$  is the excess minority carrier concentration that is generated under illumination. The higher value of charge density, in conjunction with higher quasi fermi energy, leads to a greater electron current density. Figure 3-8 (c) illustrates the electron current density enhancement in light trapping cell with respect to the bare cell. Current density that is proportional to the gradient of the quasi fermi level, shows the flow of photo generated carriers towards ohmic contacts and through the external circuit. The concentration of holes and corresponding hole current density can be explained in a similar fashion. For fair comparison, both electron density and current density (Figure 3-8 (b, c)) are integrated over the corresponding predicted I-V curve shown in the following.

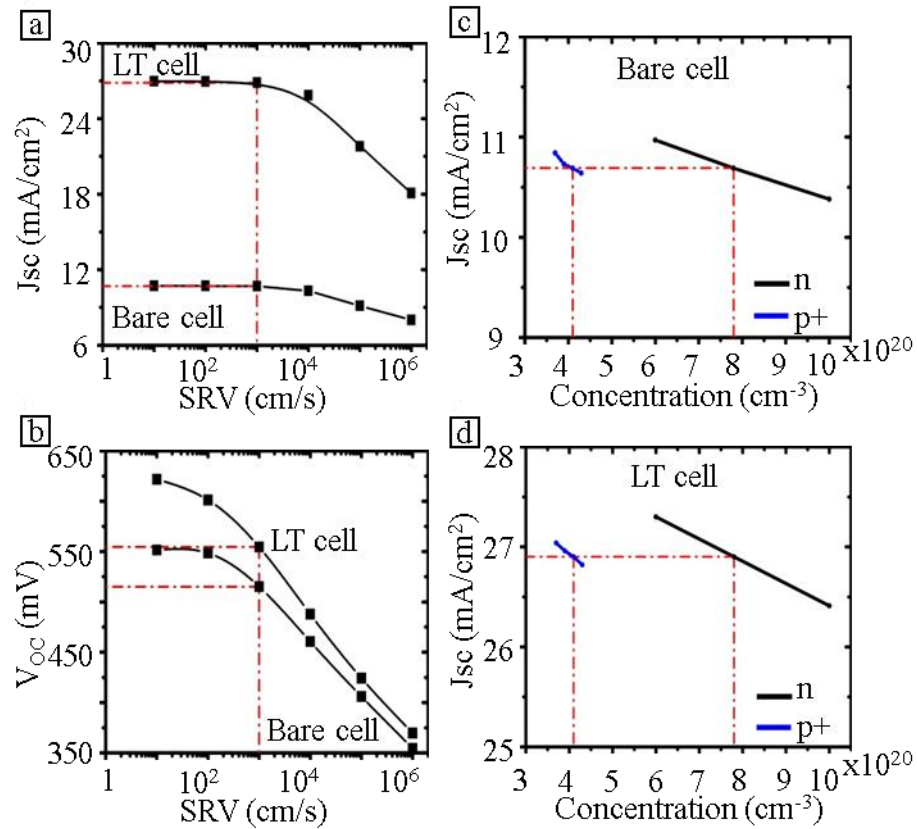


Figure 3-9 (a-b) present the predicted short circuit current density ( $J_{sc}$ ) and open circuit voltage ( $V_{oc}$ ) as a function of surface recombination velocity in the top and bottom graphs respectively, and (c-d) show the predicted short circuit current density as a function of doping concentration for both bare and light trapping cells.

Apart from the light absorption enhancement in the light trapping cell, which leads to higher internal current density as demonstrated above, it is also important to investigate the mechanisms of loss in order to improve charge collection and overall cell efficiency. The surface recombination velocity (SRV), which is one of the main sources of voltage loss and low short circuit current, defines the carrier recombination rate at the silicon interfaces due to the silicon dangling bonds. Figure 3-9 (a) shows the predicted

variation in  $J_{sc}$  as a function of SRV for bare and light trapping cells. Although, a lower SRV (1-100 cm/s)<sup>81-84</sup> produces higher  $J_{sc}$ , achieving such low SRV on a patterned surfaces of a light trapping cell requires excellent surface passivation. The impact of bulk and surface recombination on the cell performance can be described by the effective lifetime, given by<sup>81,85,86</sup>

$$\frac{1}{\tau_{eff}} = \frac{1}{\tau_{bulk}} + \frac{2SRV}{d} \quad (27)$$

where  $d$  is the cell thickness. According to the Equation (29), in lower cell thicknesses, SRV becomes more significant than the bulk lifetime. Thus a good multi-functional passivation layer on the patterned top surface which also functions as an anti-reflection coating makes a significant difference in device performance due to both photon absorption enhancement and carrier lifetime improvement. The SRV further influences the open circuit voltage which is defined in Equation (30) for a solar cell made on a p-type wafer as<sup>87-89</sup>

$$V_{OC} = \frac{KT}{q} \ln\left(\frac{J_{ph}(N_A + \Delta p)\tau_{eff}}{qdn_i^2}\right) \quad (28)$$

$$\tau_{eff} = \frac{\Delta n}{R} \quad (29)$$

where  $J_{ph}$  is photocurrent density,  $N_A$  is the acceptor concentration,  $\Delta n$  and  $\Delta p$  are the electron and hole excess minority carrier concentration respectively which are equivalent under the illumination in solar cells,  $n_i$  is the intrinsic carrier concentration, and  $R$  is the

recombination. Since SRV is inversely related to the lifetime,  $\tau_{\text{eff}}$  (Equation (29)), it reduces the open circuit voltage as can be observed in Figure 3-9 (b), and ultimately the energy conversion efficiency of the cell. Both the current density and the voltage (Figure 3-9 (a-b) of the light trapping cell decreases significantly compared to that of the bare cell as SRV increases. This sharp fall can be explained by higher surface recombination due to the surface texturing in light trapping cells. Figure 3-9 (c-d) shows the short circuit current density vs doping concentrations for boron and phosphorus regions in bare and light trapping cells respectively for the surface recombination velocity of 1000 cm/s. A SRV of 1000 cm/s is chosen for the doping concentration studies since lower SRVs can only be obtained by thermal silicon oxide growth which is not applicable in this case due to polymeric substrates of fabricated microbar cells<sup>39,59</sup>. A significant enhancement in  $J_{\text{sc}}$  can be observed in the light trapping cell compared to the bare cell. The phosphorus and boron doping concentration studied regimes are  $6\text{e}+20 - 1\text{e}+21 \text{ cm}^{-3}$  and  $3.7\text{e}+20 - 4.3\text{e}+20 \text{ cm}^{-3}$ , respectively. These variation ranges are based upon the pre-deposition furnace temperature of  $900^{\circ}\text{C} - 1050^{\circ}\text{C}$  in which the cells are exposed to the infinite constant sources<sup>90</sup>. Since our studied cell is ultrathin,  $3 \mu\text{m}$ , compared to conventional silicon solar cell thickness ( $150- 180 \mu\text{m}$ ) the drive-in diffusion process that is occurred at higher temperature ( $T > 1000^{\circ}\text{C}$ ) in the absence of the dopant source in order to increase the junction depth is not considered in this study. These results imply that lower doping concentration leads to higher current densities, at the studied doping concentration regime<sup>91</sup> which also can be shown theoretically by:

$$J_{SC} = J_0(e^{qV_{oc}/KT} - 1) \quad (30)$$

where  $J_0$  is the dark saturation current which flows through the solar cell when a bias is applied in the dark and in low level injection is given by:

$$J_0 = qn_i^2 \left( \frac{1}{N_A} \sqrt{\frac{D_n}{\tau_n}} + \frac{1}{N_D} \sqrt{\frac{D_p}{\tau_p}} \right) \quad (31)$$

$D_n, D_p$  are the electron and hole diffusion coefficients,  $\tau_n, \tau_p$  are the lifetime of electron and hole, respectively. Comparing Equation (32) and Equation (33) we can conclude that a lower doping concentration ( $N_A, N_D$ ) leads to higher  $J_0$  and consequently higher  $J_{sc}$  as observed in the numerical simulation in Figure 3-9 (c-d).

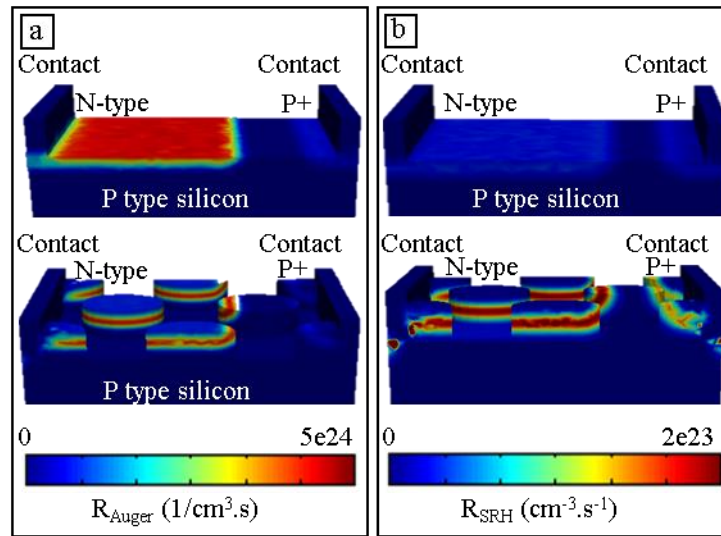


Figure 3-10 (a) and (b) compare the Auger and Shockley-Read-Hall recombination in bare and light trapping cells, respectively. Light trapping cell possesses higher recombination due to higher localized doping concentration and defect density. The cell geometry is not to scale.



Deep level or Shockley-Read-Hall (SRH) and Auger recombination are the other two carrier loss mechanisms which severely affect solar cell performance. The more heavily doped material leads to higher auger recombination and the material with more defect states has higher Shockley-Read-Hall recombination. These recombination mechanisms are defined in equations (7) and (8), chapter 1.

From Figure 3-10 (a-b) it can be seen that the light trapping cell has a higher Auger and Shockley-Read-Hall recombination rate within the posts due to the generation of higher excessive minority carriers and higher defect density, respectively. Both recombination rates are integrated over the respective I-V curve (Figure 3-11) of bare and light trapping cells in order to demonstrate the overall response. The light trapping nano-patterning introduces more localized doping distribution and more defects to the silicon cell which leads to higher auger and SRH recombination. However, enhanced absorption and carrier generation in light trapping cells compensates these recombination losses and gives a higher overall cell efficiency. Further, this work shows that the device performance can be enhanced by minimizing recombination losses via optimum doping profile and surface passivation.

### 3.2.3 Device Optimization and Simulation Parameters

The device simulation parameters are presented in the table 3-1 for two conditions: specific to the fabricated and the optimum cells. The values for the predicted cell were chosen to be either equivalent or close to the experimental conditions.

Table 3-1 The electrical simulation parameters of the fabricated (Sim.) and optimized (Opt.) bare and light trapping cells

	Wafer conc. (1/cm <sup>3</sup> )	p+ surface conc. (1/cm <sup>3</sup> )	p+ junc. width (nm)	n surface conc. (1/cm <sup>3</sup> )	n Junc. width (nm)	Electron Carrier lifetime (ms)	Hole Carrier lifetime (ms)	SRV (cm/s)	BSF conc. (1/cm <sup>3</sup> )	BSF junc. width (nm)
Opt.	10 <sup>15</sup>	3.7E+20	154	6E+20	158	1	1	10	4.1E+20	186
Sim.	10 <sup>15</sup>	4.1E+20	416	7.8E+20	140	10 <sup>-3</sup>	10 <sup>-4</sup>	10 <sup>4</sup>	4.1E+20	186

There are some discrepancies between predicted and measured cell performances primarily due to the mismatch between estimated device parameters like carrier life time, SRV, sidewall ARC thickness on the patterned surface, doping profile and actual experimental cell. The detailed light trapping pattern design and fabrication is reported previously<sup>39</sup>. Soft nanoimprint lithography (NIL) and reactive ion etching defines hexagonal cylindrical silicon posts of period 500 nm, diameter 300 nm and relief depth 140 nm as light trapping pattern which are optimized with FDTD simulation as shown in Figure 1-6. A layer of PECVD SiN<sub>x</sub> (20-50 nm) and SiO<sub>2</sub> (~50-80 nm) deposition the device serves as anti-reflection coating (ARC) and passivation layer. Different techniques of minimizing the reflection losses such as single dielectric layer, gradient refractive index layers, and nanostructured surfaces are commonly used<sup>52,54,92</sup>. A 200 nm thick gold layer serves as backside reflector (BSR). The top diffractive optics pattern functions as grating coupler to couple incoming solar radiation as diffracted/scattered modes thus enhancing effective path length. The functional cell fabrication is completed with the doping of boron and phosphorus through patterned hard masks to define the P-N junctions followed by metal contact formation as schematically shown in Fig. 1-8. These

parameters are fixed for both bare and light trapping cells in order to compare and focus on the impact of light trapping on the device performance.

Table 3-2 Short circuit current ( $J_{sc}$ ), open circuit voltage ( $V_{oc}$ ), fill factor (FF), and efficiency ( $\eta$ ) of fabricated, simulated and optimized 3  $\mu\text{m}$  bare and light trapping solar cells

	Case	$J_{sc}$ (mA/Cm <sup>2</sup> )	$V_{oc}$ (V)	<b>FF (%)</b>	<b><math>\eta</math> (%)</b>
Sim.	Bare Cell	9.8	0.5	76.4	3.73
Exp.	Bare Cell	9.6	0.45	71.1	2.9
Opt.	Bare Cell	11.4	0.64	81.8	5.95
Sim.	LT Cell	25.7	0.52	79.1	10.69
Exp.	LT Cell	24.6	0.49	71.5	8.47
Opt.	LT Cell	27.2	0.68	81.9	15.23

The predicted results and experimentally measured data<sup>80</sup> of a 3  $\mu\text{m}$  thick microbar silicon solar cell are tabulated and plotted for the comparison in table 3-2 and Figure 3-11, respectively.

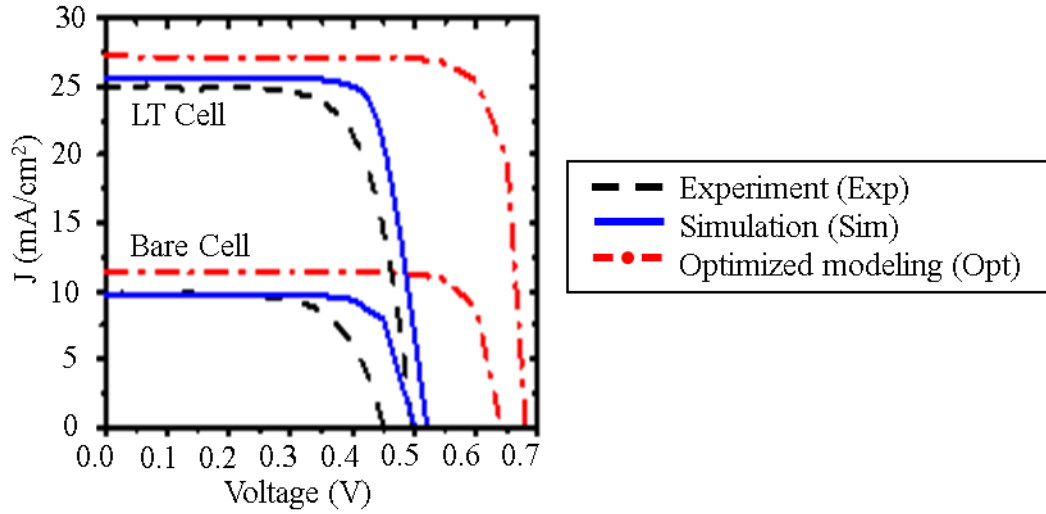


Figure 3-11 shows the corresponding I-V curves of fabricated, simulated and optimized 3  $\mu\text{m}$  bare and light trapping solar cells.

As shown in the table 3-2, the predicted  $J_{sc}$  and  $V_{oc}$  closely match experimental measurements for both bare and light trapping cells. The energy conversion efficiency enhancement prediction of 186% closely matches the experimentally measured enhancement of 192% of the light trapping cell with respect to the bare cell measurement. The main difference between the predicted and the fabricated cell is the  $V_{oc}$  that is most likely caused by non-uniform back surface field (BSF) of the fabricated cell. The optimized light trapping and bare cells show 105% and 80% percentages of improvements with respect to corresponding experimentally fabricated cells, respectively. The optimum cell design considered an ideal carrier life time and SRVs as presented in Table 3-1 in order to establish a maximum possible cell performance. For the optimized cell we used a SRV of 10 cm/s and bulk life time of 1 ms as reported in Table 3-1. Such range of low SRV and long carrier life time is indeed achievable via high quality surface

passivation<sup>50,93,94</sup>. The 3D device simulation of charge carrier generation/recombination in bare and light trapping cells in thin-film geometry in this study distinctively showed the inter-relation between various processes. The study also defined parameter space (doping profile, junction depth, SRV etc.) for optimum performance of a 3  $\mu\text{m}$  thick light trapping solar cell. The future work will focus on bridging the gap between the present and the optimal cell performances following this unified electromagnetic-electronic design approach presented above.

### 3.3 Methods

The fabrication starts with surface patterning on  $\langle 111 \rangle$  p-type c-Si by imprinting method that is described in chapter 1, Figure 3-12. Then 500 nm  $\text{SiO}_2$  is deposited to mask silicon surface using PECVD Trion Orion II with Tetraethyl orthosilicate TEOS He bubbler at 300 °C and 100 sccm  $\text{O}_2$ , 30 sccm TEOS, 900 mTorr pressure, 100 W RF power with deposition rate of  $\sim 1$  nm/sec. Then the micro-bars pattern is formed perpendicular to  $\langle 110 \rangle$  direction on the wafers using a photolithography step followed by wet etching of exposed  $\text{SiO}_2$  in buffered oxide etch (BOE) or 10% diluted hydrofluoric acid (HF) and using deep RIE etcher STS system, with 130 sccm  $\text{SF}_6$ , 13 sccm  $\text{O}_2$  (7 sec each cycle), 110 sccm  $\text{C}_4\text{F}_8$  (5 sec each cycle), 800 W coil power, 20 W platen power, and 15 mTorr pressure to etch 3.2  $\mu\text{m}$  of exposed silicon in the trenches. The oxide mask is removed in HF. A new 500 nm  $\text{SiO}_2$  layer is deposited as a mask using PECVD with the same recipe to form n-region on the bars. Phosphorus doping is done at 950 °C for 12 minutes with PH-1000 Saint-Gobain solid sources. The oxide layer is removed afterwards and a new

oxide layer deposited to serve as a mask for p+-region formation. Boron doping is performed at 900 °C for 20 minutes with BN-975 Saint-Gobain solid sources. The mask layer is removed. Then 100 nm SiO<sub>2</sub>, and 500 nm Si<sub>3</sub>N<sub>4</sub> is deposited using Plasma-Therm 790 PECVD using described recipes in chapter 2. Two angled Cr/Au (5 nm/100 nm) is deposited using electron beam evaporator to cover the top and sidewalls of micr-bars but leave without any metal deposition on the trenches in between the bars. Next, the nitride layer deposited is etched using low frequency reactive ion etching system (Trion minilock) with 50 sccm SF<sub>6</sub> and 5 sccm O<sub>2</sub>, 300 W icp power, 200 W RIE power and 100 mTorr pressure with the etch rate of 3-4 nm per sec and the oxide layer is removed etched in BOE. Then the wafer is soaked in potassium hydroxide (KOH) for anisotropic etching of silicon at 100 °C for 40 minutes until the silicon bars are undercut and only anchored from both ends. The metals are removed in metal etchant and a p+ doping process is done for the bottom side of the bars at 900 °C for 20 minutes. nitride layer is removed using RIE. The released bars are transfer printed with PDMS stamp onto a glass slide coated with a transparent photo curable polyurethane (NOA 61) followed by ultra-violet exposure for 30 minutes. Then the PDMS stamp is released. At the end, metal contacts are formed by a photolithography step and Cr/Au (5 nm/200 nm) evaporation and lift-off.

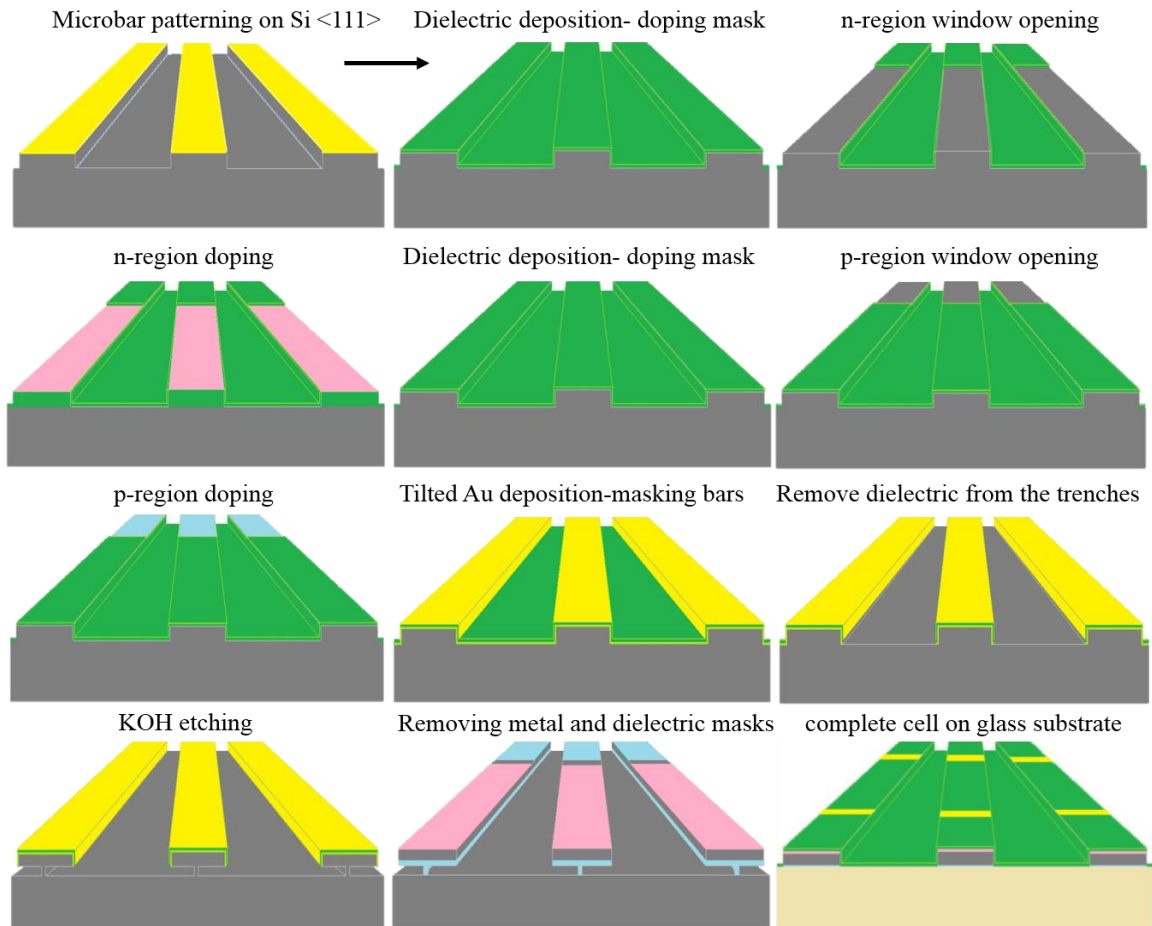


Figure 3-12 shows the fabrication process of making 3  $\mu\text{m}$  thick micro-bar solar cell on  $\langle 111 \rangle$  silicon wafer from the beginning (top left) to the end (bottom right). The direction to follow the process is shown with an arrow in the first row.

Figure 3-13 illustrates a SEM image of released microbars anchored to the substrate from both ends (left), and an optical image of transfer printed microbars onto a glass substrate before formation of contacts (right).

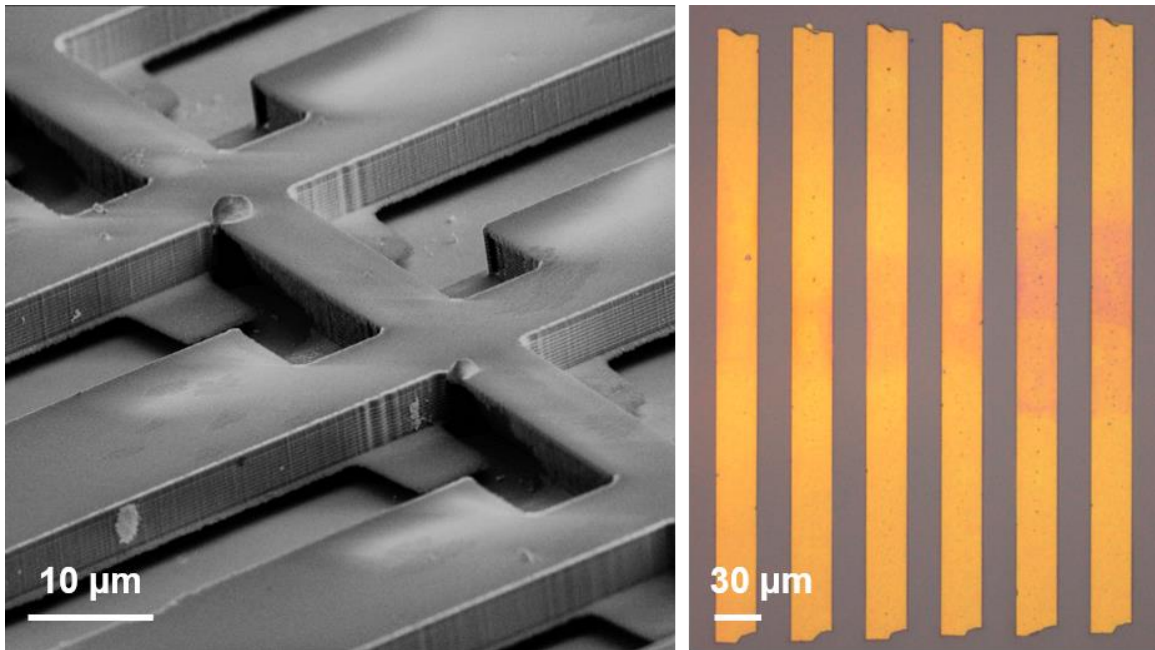


Figure 3-13 shows a SEM image of under-cut silicon microbars (left) and an optical image of transfer printed microbars onto a glass substrate (right).

### 3.4 Conclusion

We theoretically studied 3 μm thick light trapping cell in order to show what can be achieved in terms of device performance following unified design approach. The light trapping scheme showed significant enhancement in band edge photon absorption resulting in higher charge carrier generation rate. It is graphically demonstrated that higher generation rate leads to higher current density. It is shown that surface recombination velocity has a large impact on short circuit current density ( $J_{sc}$ ) and more significantly open circuit voltage ( $V_{oc}$ ) meaning that a good passivation is a must for high efficiency achievements. The predicted short circuit current density as a function of doping concentration for both bare and light trapping cells shows that very heavy doping concentration result in lower current generation since the charge carriers rapidly



recombine at the surface. Although nano-patterning causes more recombination, its impact on the overall cell efficiency enhancement is significant due to the stronger light absorption and higher generation rate which outweighs recombination losses. Such a unified electromagnetic-electronic design approach will help design better solar cell architecture with higher energy conversion efficiency.

## CHAPTER 4      FUNCTIONAL LIGHT TRAPPING CELLS

### 4.1    Introduction

In previous chapters, the significant role of applying advanced light trapping designs on thin film silicon solar cells is discussed. In this chapter we discuss implementation of the light trapping approach that is established and optimized, as shown earlier in this thesis, on 20  $\mu\text{m}$  silicon solar cells in conjunction with characterization of 100  $\mu\text{m}$  silicon solar cells with and without the surface nano-patterning approach. The choice of 20  $\mu\text{m}$  thickness in this work gives the benefit of higher yield and absorption of sunlight, >90%. On the other hand 100  $\mu\text{m}$  cells are easier in handling for the fabrication process, and it allows us to use characterization tools such as external quantum efficiency and lifetime measurements systems to investigate cell performance and loss mechanisms. The spatial absorption profile of the light trapping  $\mu\text{m}$  cell is predicted in comparison with sun spectrum and an equivalent bare cell absorption profile using FDTD simulations. Since the recombination has a significant impact on the wafer's carrier lifetime, the open-circuit voltage and efficiency of a bare and light trapping 20  $\mu\text{m}$  silicon solar cells are predicted as a function of silicon bulk's carrier lifetime. The short circuit current ( $J_{sc}$ ), open circuit voltage ( $V_{oc}$ ) and efficiency ( $\eta$ ) from an optimized doping profile and carrier life time are predicted for bare and patterned cell as well. We experimentally show that there is an enhancement in  $J_{sc}$  and hence the efficiency of the patterned cells with respect to un-patterned bare cell.

## 4.2 Results and Discussion

A 100  $\mu\text{m}$  and 20  $\mu\text{m}$  light trapping silicon solar cell design architecture is shown in Figure 4-1 (a) and (b) respectively. In both devices, silicon is patterned with the top diffractive nano-structures, SEM image in Figure 4-1 (a), and coated with an index matched dielectric layer. Aluminum as the rear metal electrode acts as backside reflector as well. Using silicon-on-insulator (SOI) wafer to fabricate 20  $\mu\text{m}$  cells facilitates the device handling.

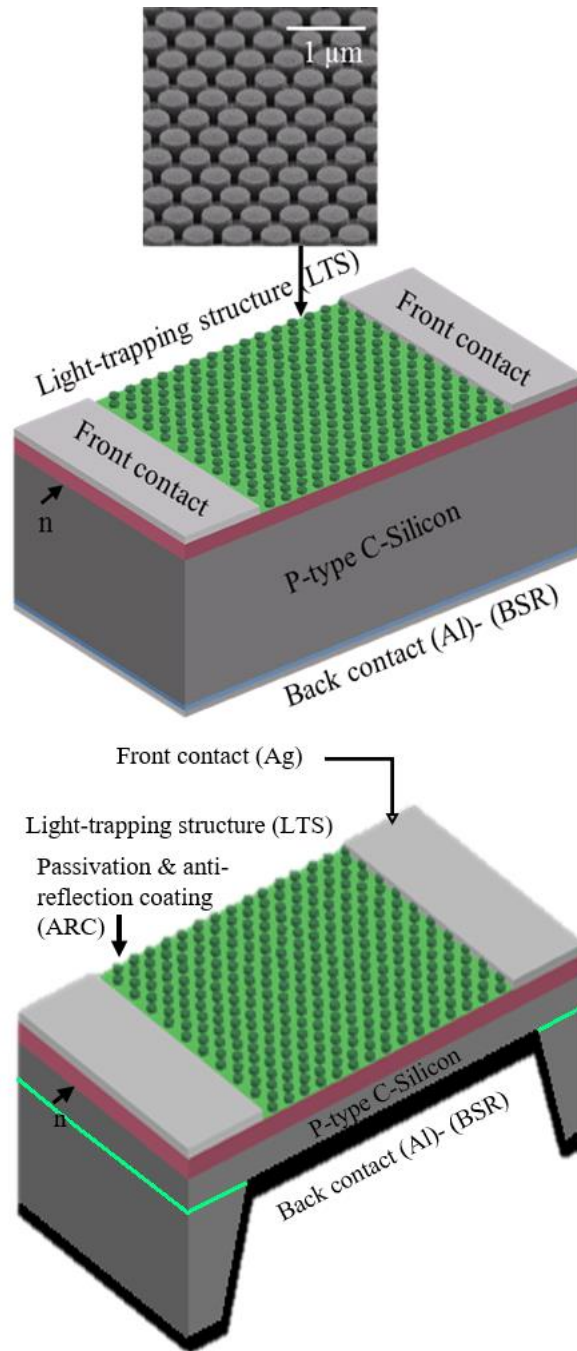


Figure 4-1 shows light trapping c-Si solar cell architecture of 100 μm (a) and (b) 20 μm cell that is fabricated on a silicon-on-insulator (SOI) wafer.

The numerically predicted spatial absorption profile of the 20  $\mu\text{m}$  solar cell with and without the light trapping structure is compared with respect to the AM1.5G spectrum in Figure 4-2. It is shown that 91% integrated absorption of the integrated sun spectrum can be achieved in the 20  $\mu\text{m}$  light trapping cell compare to 57% absorption of the equivalent bare cell. Since, the absorption of 100  $\mu\text{m}$  silicon with an optimized anti-reflection coating and backside reflector is  $>90\%$ , the top diffractive pattern may not add as much to the optical performance of such a thick cell. Previously optimized 2D hexagonal array of posts of period (P) 500nm, diameter to period ratio (D/P) 0.6 and relief depth (RD) 140 nm is used in this work as the top diffractive pattern.

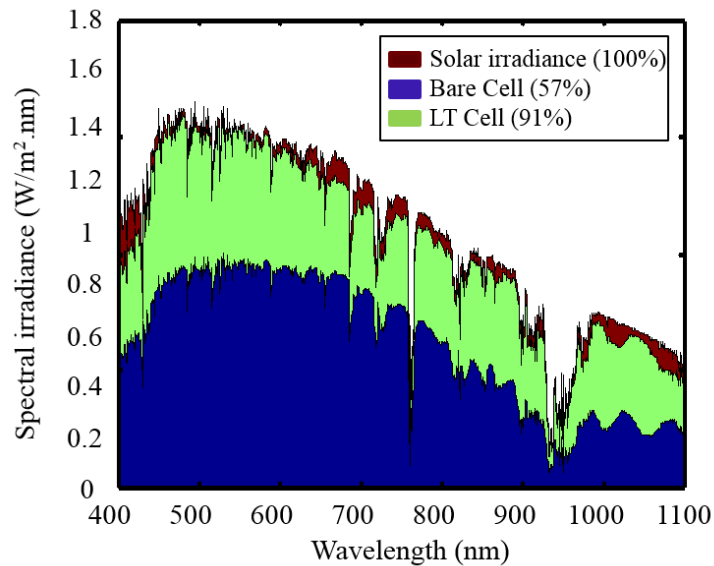


Figure 4-2 illustrates the comparison between the integrated absorption of 20  $\mu\text{m}$  c-Si solar cell with and without light trapping with respect to the solar spectrum.

Additional to the optical characterization of the light trapping cells, we also performed the external quantum efficiency measurement to analyze the incident photons'

collection, Figure 4-3. The EQE measurement results show that there are losses such as front surface recombination at shorter wavelengths (blue response), rear surface recombination, reduced absorption and low diffusion length at longer wavelengths (red response), and low diffusion length and reflection which reduce the overall quantum efficiency in solar cells otherwise ideally this value should be unity for the photons with energies above the bandgap if each incident photon get absorbed and collected.

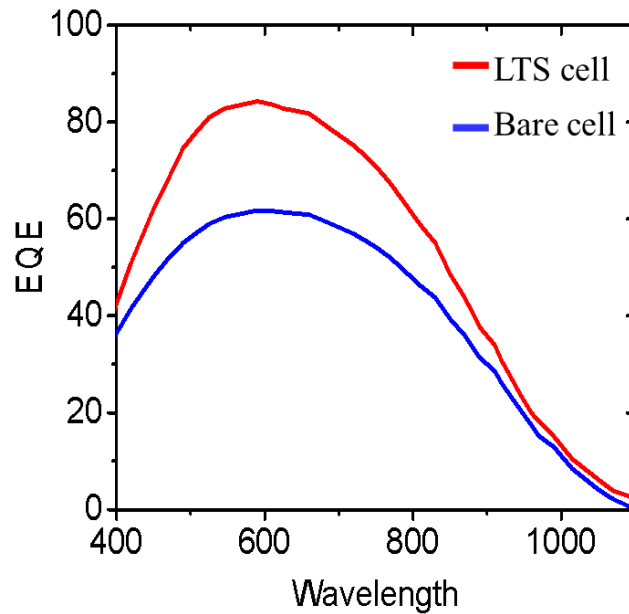


Figure 4-3 presents external quantum efficiency measurement of a 100  $\mu\text{m}$  bare and patterned cell, both with ARC and BSR.

From the EQE curves, diffusion length is one of the main loss mechanisms that is directly proportional to the carrier lifetime (or inversely proportional to the recombination rate). The surface recombination is studied in chapter 3 and it is concluded that having high quality surface passivation can minimize the surface recombination

effects on a cell performance. Hence, here we investigated bulk recombination by modeling the impact of silicon bulk carrier lifetime on short-circuit current ( $J_{sc}$ ), open-circuit voltage ( $V_{oc}$ ) and efficiency ( $\eta$ ) for both 100  $\mu\text{m}$  bare and light trapping cell, Figure 4-4 (a-c). The simulation is done by importing the predicted 3D generation rate data into the numerical electronic modeling (Lumerical DEVICE, Lumerical Inc.). A sharper fall in  $V_{oc}$  for light trapping cell is observed that is due to higher surface recombination caused by the surface texturing, Figure 4-4 (b). Predicted  $V_{oc}$  and  $\eta$  for 20  $\mu\text{m}$  c-Si solar cell with and without top diffractive pattern is consistent with the results from 100  $\mu\text{m}$  cell, Figure 4-4 (d). Low quality wafers or any sorts of contamination and/or defects which introduce high deep level recombination into the silicon bulk especially at high temperature fabrication steps can cause degradation of bulk lifetime as a result, equation (31) which has a significant impact on the charge collection and energy conversion efficiency. Figure 24 shows for both bare and light trapping cell there is a 150 mV and 100 mV open-circuit voltage difference between 1 msec and 1  $\mu\text{sec}$  lifetime values for 100  $\mu\text{m}$  and 20  $\mu\text{m}$  cells respectively which can be verified with equation (30). It is also shown that the efficiency in both cells can be improved up to 25% as the lifetime increases from 1  $\mu\text{sec}$  to 1 msec, (right to left). The surface recombination velocity (SRV) in this simulation is constant and chosen to be 1000 cm/s since lower SRVs require excellent surface passivation. In both cells an optimized single layer anti-reflection, chapter 2, coating is considered.

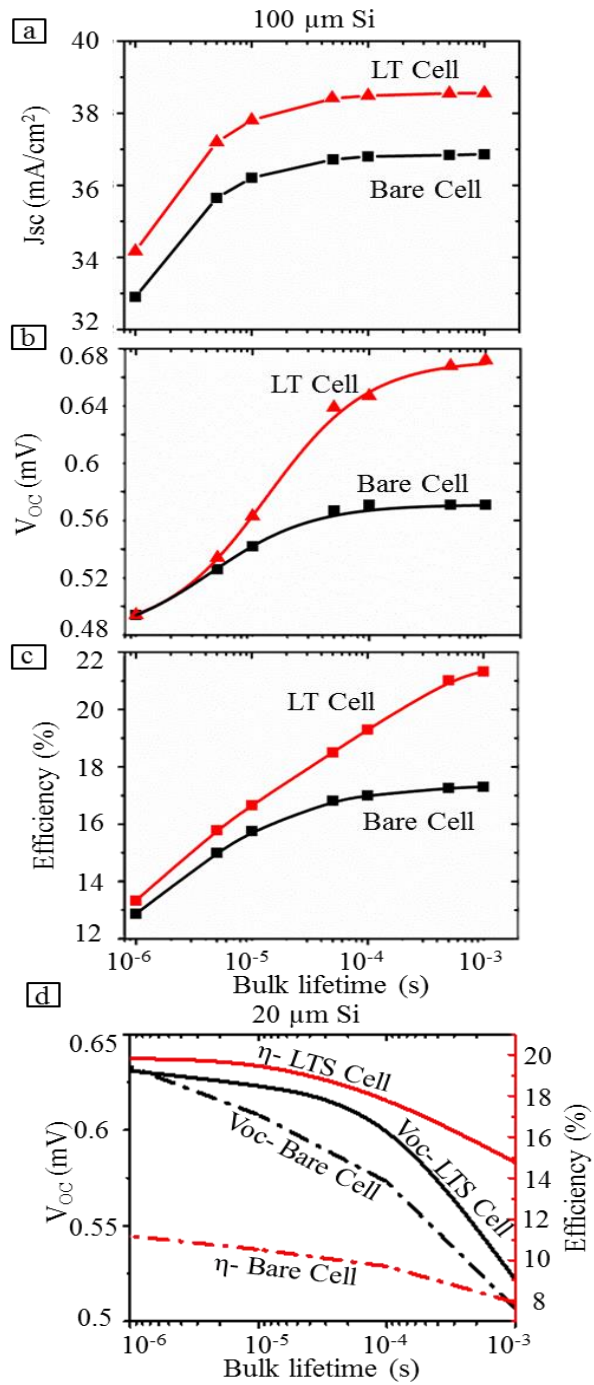


Figure 4-4 presents the impact of bulk lifetime on  $J_{sc}$  (a)  $V_{oc}$  (b) and  $\eta$  (c) in 100  $\mu\text{m}$  cell. (d) Predicted  $V_{oc}$  and  $\eta$  vs bulk lifetime for 20  $\mu\text{m}$  cell verifies the results in (a).



The experimentally measured data of 100  $\mu\text{m}$  cells and predicted optimized parameters for a near perfect cell are presented in Table 4-1 and Figure 4-5 respectively.

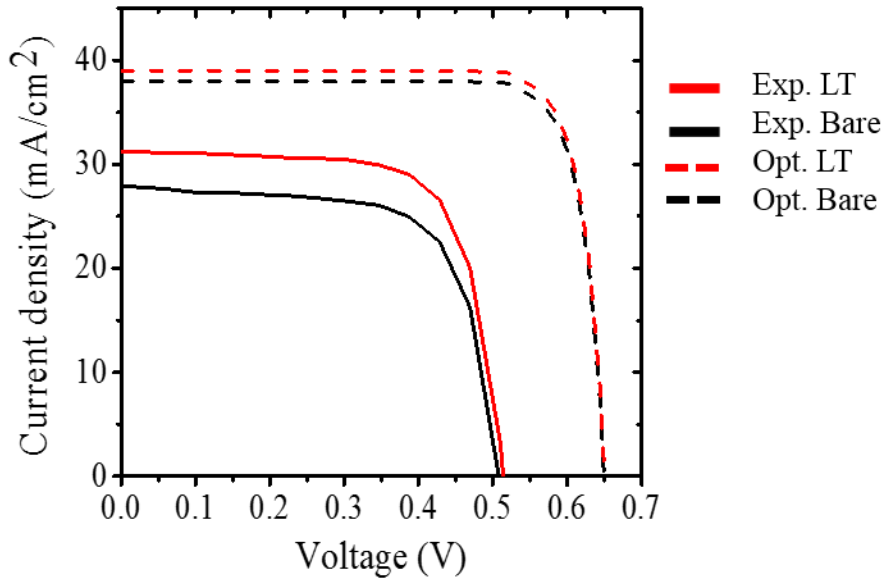


Figure 4-5 presents the I-V curves of experimental (solid lines) and predicted data (dash lines) for a 100  $\mu\text{m}$  bare (black) and a patterned solar (red) cell.

Table 4-1 Short circuit current ( $J_{sc}$ ), open circuit voltage ( $V_{oc}$ ), fill factor (FF), and efficiency ( $\eta$ ) of fabricated and optimized 100  $\mu\text{m}$  bare and patterned solar cells

100 $\mu\text{m}$	Case	$J_{sc}$ ( $\text{mA}/\text{Cm}^2$ )	$V_{oc}$ (V)	FF (%)	$\eta$ (%)
Exp.	Bare Cell	27.9	508	69.1	9.8
Exp.	LT Cell	32.2	514	71.35	11.45
Opt.	Bare Cell	38	649	82	20.25
Opt.	LT Cell	39.1	650	81.9	20.82

Table 4-2 and Figure 4-6 show the predicted and experimental result of 20  $\mu\text{m}$  in the same fashion.

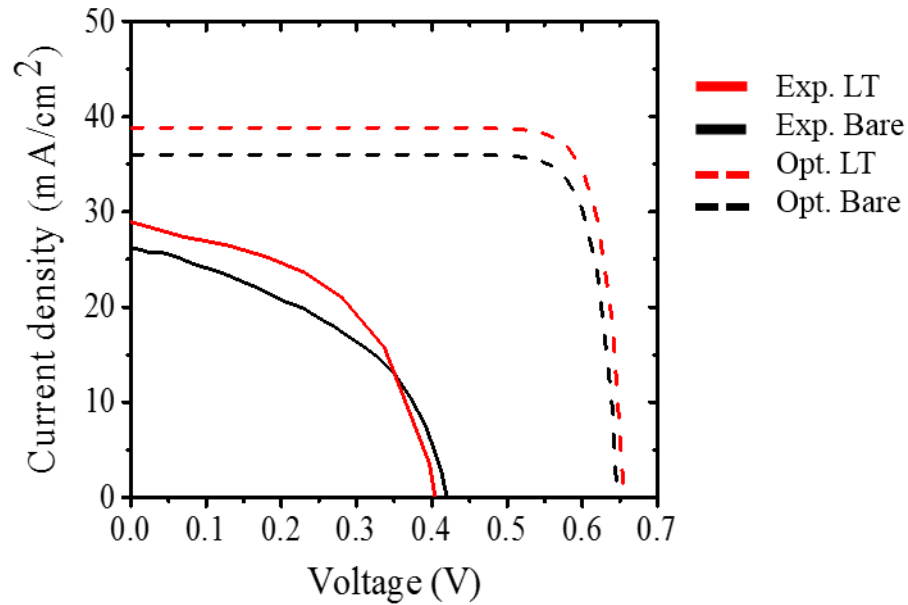


Figure 4-6 presents the I-V curves of experimental (solid lines) and predicted data (dash lines) for a 20  $\mu\text{m}$  bare (black) and a patterned solar (red) cell.

Table 4-2 Short circuit current ( $J_{sc}$ ), open circuit voltage ( $V_{oc}$ ), fill factor (FF), and efficiency ( $\eta$ ) of fabricated and optimized 20  $\mu\text{m}$  bare and patterned solar cells

20 $\mu\text{m}$	Case	$J_{sc}$ (mA/Cm2)	$V_{oc}$ (V)	FF (%)	$\eta$ (%)
Exp.	Bare Cell	26.2	420	44.5	4.9
Exp.	LT Cell	30	405	58.8	6.9
Opt.	Bare Cell	36	645	76.2	17.7
Opt.	LT Cell	38.9	658	76	19.4

In the optimized design a heavy doping is considered under the front and rear contacts in order to obtain higher carrier collection while maintaining a good surface passivation, Table 4-3. The rear contact is localized through a dielectric passivation layer. Near perfect bulk lifetime (1 msec) and SRV (1-100 cm/sec) are the assumptions of the

optimized cell. However, the localized doping processes for the contact regions are skipped in our fabricated cells to prevent complications in fabrication process. The doping levels in this condition serve for both contact and absorbing regions.

Table 4-3 The electrical simulation parameters of the optimized (Opt.) bare and patterned solar cells

	Wafer conc. (1/cm <sup>3</sup> )	p+ surface conc. (1/cm <sup>3</sup> )	p+ junc. width (nm)	n+ surface conc. (1/cm <sup>3</sup> )	n+ Junc. width (nm)	Carrier lifetime (ms)	Metal SRV (cm/s)	SRV (cm/s)	Front contact area (%)	n surface conc. (1/cm <sup>3</sup> )	n Junc. width (nm)
Opt. Bare	10 <sup>16</sup>	1E+20	200	3E+20	200	1	100	1	10	5E+19	500
Opt. LT	10 <sup>16</sup>	1E+20	200	3E+20	200	1	100	1	10	5E+19	500

The inconsistency between the experimentally fabricated and optimized cell in Figures 4-5 and 4-6 is partially due to the non-localized doping by making the decision of reducing the fabrication process. However, the major loss between the experimental and ideal cell can be explained by the results of recombination losses which are previously presented in Figures 3-9 and 4-4. In order to validate this claim, bulk lifetime measurement is conducted on two type of wafers before and after doping that is a high temperature process using Sinton WCT-120 system which works based on electro-magnetic induction using a sensor and a filtered xenon flash lamp. One is the 100  $\mu\text{m}$  p-type silicon wafers on which the presented solar cells are fabricated. Second one is a 200  $\mu\text{m}$  n-type silicon wafer with few nanometers of thermally grown silicon oxide. Both wafers are then passivated with Al<sub>2</sub>O<sub>3</sub> and SiN<sub>x</sub> followed by annealing at 430 °C for 30 minutes shortly

before bulk lifetime measurement. According to the measured data, shown in Table 4-4, lifetime of both wafers are dropped by an order of magnitude after the doping process which is done at 900 °C for 20 minutes. At such a high temperature any contaminant material such as metals diffuse into the bulk of semiconductor into which introduce defects. Thus the current density, voltage and fill factor are impacted significantly by recombination in bulk of silicon and at the surface (especially at non-passivated rear side in the experiments).

Table 4-4 The lifetime measurement results for 100  $\mu\text{m}$  and 200  $\mu\text{m}$  c-Si wafers.

Sample	Film thickness ( $\mu\text{m}$ )	Resistivity ( $\Omega\text{-cm}$ )	$J_0$	1 sun implied $V_{oc}$ (V)	Lifetime ( $\mu\text{s}$ )
Original	100	1	1.2E-13	0.65	137.35
Doped	100	0.53	4.8E-13	0.52	13.51
Original	200	2.36	2E-14	0.7	1395
Doped	200	0.34	5.6E-13	0.67	139

### 4.3 Methods

#### 4.3.1 100 $\mu\text{m}$ Cell Fabrication

The process starts with patterning the top surface of 100  $\mu\text{m}$  p-type, 1-30 ohm-cm, <100> silicon wafer by soft nano-imprinting lithography followed by MaCEtch process that is described earlier in chapter 2. Once the desirable relief depth is obtained the wafer is cleaned. Rear side of the wafer is masked with >500 nm silicon oxide deposited by PECVD Trion Orion II system with the same recipe described in chapter 3.

The phosphorus doping is done at 900 °C for 20 minutes. The masking oxide layer is chemically removed with BOE or diluted HF. Another >500 nm oxide layer is deposited using PECVD to mask the front side followed by boron doping at 900 °C for 20 minutes. A diffusion process takes place afterwards at 1100 °C for 10 minutes (It is found that drive-in at 1000 C for 30 minutes is more efficient). The oxide mask is etched in BOE /HF 10 %. Then the front side is passivated by 50 nm SiNx deposition by a Plasma-Therm 790 plasma PECVD system at 300 °C with the same recipe that is described in chapter 2. Front contacts are patterned through a photolithography step followed by dry etching the silicon nitride using low frequency RIE system (Trion minilock) with the recipe used in chapter 3. Next, 35 nm titanium (Ti) as adhesion layer, 35 nm palladium (Pd) as transition layer<sup>44</sup> and 500 nm Silver (Ag) is deposited using electron beam evaporator at 10<sup>-6</sup> Torr pressure and the metal coated photoresist is lifted off in acetone. Finally 2 μm Al layer is deposited to form the rear contact.

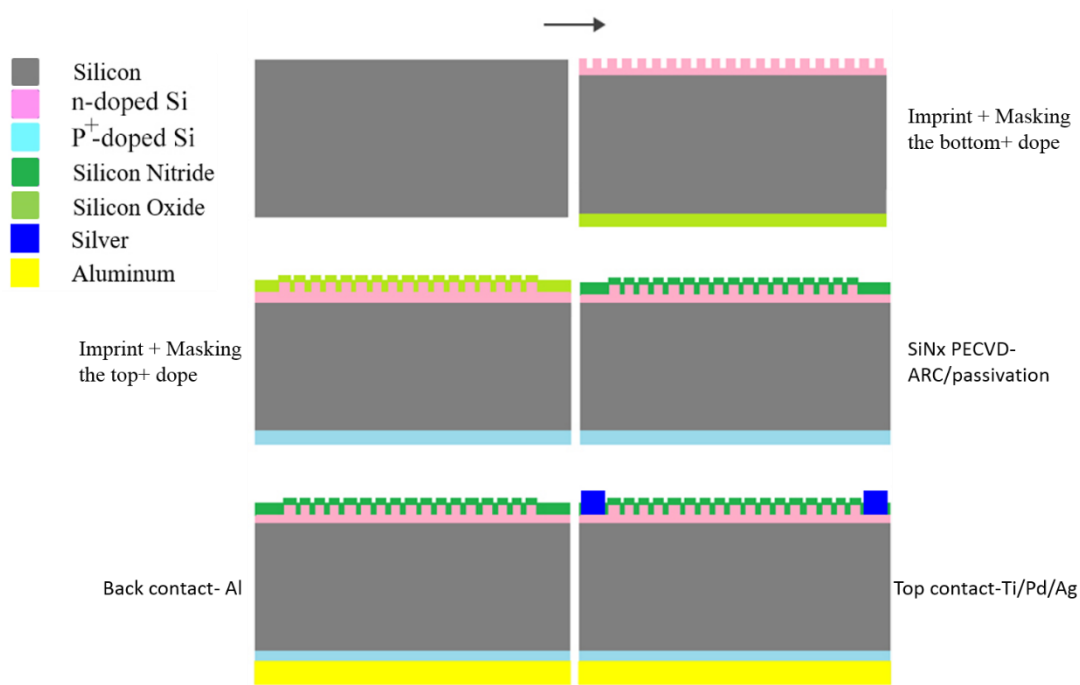


Figure 4-7 shows the fabrication process of making 100 μm solar cell on <100> p-doped double side polished Si wafer from the beginning (top left) to the end (bottom right). The direction to follow the process is shown with an arrow in the first row.

#### 4.3.2 20 μm Cell Fabrication

Figure 4-8: Solar cell device is fabricated on a 3 inch silicon-on-insulator (SOI) wafer with 20 μm p-type,  $\rho = 1-5 \Omega \text{ cm}$  device layer, 0.5 μm silicon oxide that is buried underneath the device layer and 350 μm silicon handle layer. The fabrication starts with the same surface patterning process as is done for 100 μm cell. The wafer goes through a phosphorous doping process at 900 °C for 20 minutes. A 50 nm Si<sub>3</sub>N<sub>4</sub> layer is deposited using PECVD technique with gasses at 300 °C on the device layer as an anti-reflection coating with the same recipe that is used in chapter 2. Then 3.5 μm SiO<sub>2</sub> layer is deposited on the handle side to serve as a hard mask for backside deep RIE etching by following the recipe in 100 μm cell fabrication. Front contact is formed by a

photolithography step followed by deposition of 35 nm Ti, 35 nm Pd, and 500 nm Ag and lift-off in acetone. Each cell has  $5 \times 5 \text{ mm}^2$  active area plus  $5 \times 1 \text{ mm}^2$  contact area. The rear contact window is defined by photolithography that is slightly smaller than the cell's total area. Then the  $350 \text{ }\mu\text{m}$  silicon handle layer is etched through the rear contact window in a bosch process<sup>95</sup> by using deep RIE etcher STS system, with 130 sccm  $\text{SF}_6$ , 13 sccm  $\text{O}_2$  (7 sec each cycle), 110 sccm  $\text{C}_4\text{F}_8$  (5 sec each cycle), 800 W coil power, 20 W platen power, and 15 mTorr pressure until the buried oxide layer is exposed. The etch rate of  $0.5 \text{ }\mu\text{m}$  per cycle is obtained. The front side of the cells on device layer is masked with photoresist during the backside etching process that is also used in another dry etching process on the device layer to electrically isolate each cell from the adjacent cells.  $1\text{-}2 \text{ }\mu\text{m}$  Al layer deposited as the rear contact after removing the exposed buried oxide layer from the rear window using 10% HF. The photoresist mask is removed at the end.

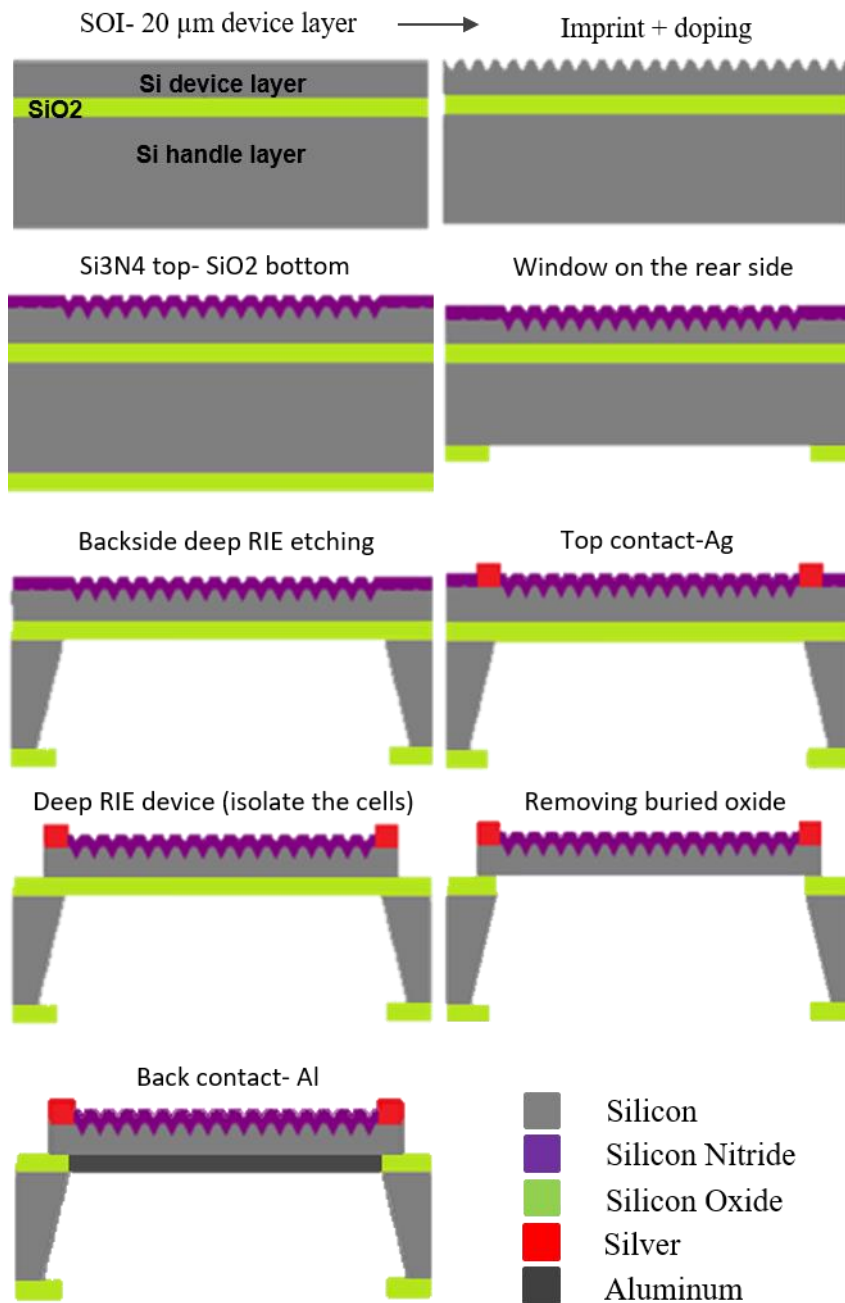


Figure 4-8 shows the fabrication process of making 20  $\mu\text{m}$  solar cell on SOI wafer from the beginning (top left) to the end (bottom left). The direction to follow the process is shown with an arrow in the first row.



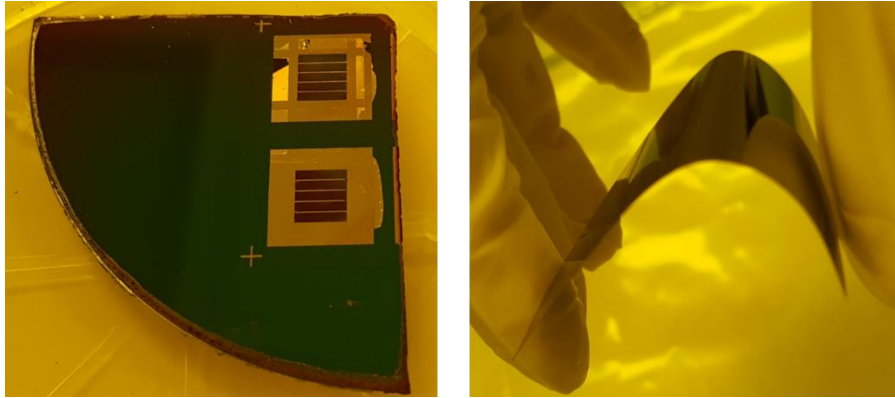


Figure 4-9 (left) shows the fabricated 20  $\mu\text{m}$  solar cell on SOI wafers, (right) shows the flexibility of a thin Si.

#### 4.4 Conclusion

100  $\mu\text{m}$  and 20  $\mu\text{m}$  mono-crystalline silicon solar cells are fabricated with two different approaches and characterized. This work predicts 60 % enhancement in photon absorption of 20  $\mu\text{m}$  thick light trapping cell compare to an equivalent bare one using FDTD simulations. This enhancement becomes weaker as silicon thickness increases. Then to study bulk recombination loss, the impact of carrier lifetime in the bulk of silicon on the bare and light trapping cell performance is predicted for both 100  $\mu\text{m}$  and 20  $\mu\text{m}$  cells using Lumerical Device modeling. The results which are consistent for both cases show a significant enhancement in open-circuit voltage ( $V_{oc}$ ) and efficiency ( $\eta$ ) from micro-sec to mili-sec lifetime values. The short-circuit current ( $J_{sc}$ ), open-circuit voltage ( $V_{oc}$ ) and efficiency ( $\eta$ ) is predicted for near perfect 20  $\mu\text{m}$  c-Si solar cell with and without top diffractive pattern in order to show the maximum possible cell performance at this thickness. There is 8% and 9.6 % predicted enhancement in  $J_{sc}$  and  $\eta$  of a well passivated (with ARC) patterned silicon with respect to an un-patterned one. Therefore,

we fabricated and measured 20  $\mu\text{m}$  c-Si solar cells with and without surface nano-patterning. A doping experiment is performed on two types of silicon wafers while minimizing surface passivation impact for bulk lifetime measurement in order to verify the simulations and identify the main loss mechanism in the fabricated cells. The result shows an order of magnitude reduction in both types of silicon wafers which significantly lower the current and voltage of the cells. The experimental results also show short-circuit current and efficiency enhancement in the patterned cell due to the higher photon absorption with respect to the un-patterned cell. Although this enhancement is more significant in 20  $\mu\text{m}$ , multiple lithography steps are required in order to target the optimum efficiency which makes the fabrication more complicated than 100  $\mu\text{m}$  cells.

## CHAPTER 5 CONCLUSION

A 2D hexagonal Bravais lattice as top diffractive pattern for thin film crystalline silicon solar cell applications is presented. To maximize the absorption of sunlight spectrum in thin film silicon device, the pattern geometry is optimized using Fourier difference time domain (FDTD) simulation technique. The wavelength integrated absorption of patterned silicon combined with anti-reflective coating (ARC) and backside reflector (BSR) in comparison with an equivalent un-patterned silicon as a function of thickness shows that the 3  $\mu\text{m}$  light trapping silicon solar cell absorbs ~80 % of solar spectrum while 3  $\mu\text{m}$  bare silicon only absorbs 36 % of the sunlight. In order to achieve > 90 % absorption, 20  $\mu\text{m}$  thick silicon is required implemented with light trapping combination.

Broadband, angle independent anti-reflection coating for use on nanostructured solar cells is optimized using FDTD simulation and experimentally validated by presenting the normal incident and angle resolved reluctance spectra that are obtained using Fourier transform infrared (FTIR) spectrometer and Reflectance/Transmittance integrating sphere respectively. Three single layer and a bi-layer ARC on patterned and bare silicon is studied numerically and experimentally for conformal and non-conformal coatings. According to the results, lower step coverages result in a lower wavelength integrated reflectance in comparison with conformal coatings. Silicon nano-structures are fabricated using soft nano-imprinting lithography followed by meat-assisted-chemical etching technique. For the experimental single layer ARC study,  $\text{Al}_2\text{O}_3$  is deposited by ALD, and  $\text{Si}_3\text{N}_4$  and  $\text{SiO}_2$  are deposited by PECVD. The minimum integrated reflectance

is predicted to be 2.2% for 60 nm  $\text{Si}_3\text{N}_4$  single layer and 1.5% for bi-layer ARC, 70 nm  $\text{Si}_3\text{N}_4$ - 100 nm  $\text{SiO}_2$ , on patterned silicon over a range of wavelengths. Moreover, it is shown that the optimized bi-layer ARC is significantly independent of the angle of incident, <4% integrated reflectance up to  $60^\circ$ , that is very competitive for solar cell applications.

3  $\mu\text{m}$  thick light trapping micro-bar shape solar cell is theoretically investigated in order to optimize the device performance. Simulation results shows 117% enhancement in photon absorption in the 3  $\mu\text{m}$  light trapping cell which leads to higher charge carrier generation rate. It is shown that surface recombination in silicon which can be controlled by variety of passivation techniques has a significant impact on a solar cell performance. Although surface patterning can potentially be a source of recombination due to introducing defects and larger number of photo-generated carriers, the prediction shows 156% efficiency enhancement can be achieved with optimized doping profile and well passivated surface.

A 100  $\mu\text{m}$ , and a 20  $\mu\text{m}$  light trapping c-Si solar cell are modeled, fabricated and characterized in comparison with equivalent un-patterned cells. 100  $\mu\text{m}$  thick cell is fabricated for characterization purposes due to less fabrication steps and easier handling and the 20  $\mu\text{m}$  thick cell is fabricated on silicon-on-insulator wafers that gives >90% yield. The FDTD simulations predict 60% photon absorption enhancement in 20  $\mu\text{m}$  light trapping cell with respect to an equivalent bare cell. Experimentally measured I-V curve also shows current density and efficiency enhancement as well. For characterization purposes, short-circuit current ( $J_{sc}$ ), open-circuit voltage ( $V_{oc}$ ) and efficiency ( $\eta$ ) as a

function of bulk lifetime is studied using Device modeling software to show the influence of defects on cell's performance. The result shows that these parameters are significantly dependent on the bulk quality of the silicon wafers.

In order to study a wafer quality through the fabrication process, a doping experiment is performed in two types of well passivated silicon wafers to characterize the bulk lifetime of the wafers before and after the doping as a high temperature process. The lifetime measurement of both wafers decreased by an order of magnitude from the original measurements before doping process. This drastic degradation leads to significantly lower current and voltage in the cells. It is concluded that good consistency between simulation and measurements requires high quality doping process.

Finally, it is shown that high efficiency ultra-thin film solar cells can be achieved by applying the studied light trapping scheme and maintaining the quality of surface and bulk of silicon as high as possible. By implementing this light trapping approach ultra-thin silicon solar cells screen printed on large scale sheets of plastics, light weight and flexible modules, can be produced which not only leads to more cost effective and easier installation process but also increases the capabilities in mobile applications.

## LIST OF REFERENCES

- 1 Hegedus, S. & Luque, A. in *Handbook of Photovoltaic Science and Engineering* 1-38 (John Wiley & Sons, Ltd, 2011).
- 2 Blakers, A. W. & Green, M. A. 20% efficiency silicon solar cells. *Applied Physics Letters* **48**, 215-217, doi:10.1063/1.96799 (1986).
- 3 Bagnall, D. M. & Boreland, M. Photovoltaic technologies. *Energy Policy* **36**, 4390-4396, doi:10.1016/j.enpol.2008.09.070 (2008).
- 4 Saga, T. Advances in crystalline silicon solar cell technology for industrial mass production. *NPG Asia Materials* **2**, 96-102, doi:10.1038/asiamat.2010.82 (2010).
- 5 Wang, A., Zhao, J. & Green, M. A. 24% efficient silicon solar cells. *Applied Physics Letters* **57**, 602, doi:10.1063/1.103610 (1990).
- 6 Dimroth, F. High-efficiency solar cells from III-V compound semiconductors.
- 7 Hoppe, H. & Sariciftci, N. S. Organic solar cells: An overview. *Journal of Materials Research* **19**, 1924-1945, doi:10.1557/jmr.2004.0252 (2011).
- 8 Green, M. A., Ho-Baillie, A. & Snaith, H. J. The emergence of perovskite solar cells. *Nature Photonics* **8**, 506-514, doi:10.1038/nphoton.2014.134 (2014).
- 9 Mandal, P. & Sharma, S. Progress in plasmonic solar cell efficiency improvement: A status review. *Renewable & Sustainable Energy Reviews* **65**, 537-552, doi:10.1016/j.rser.2016.07.031 (2016).
- 10 Law, M., Greene, L. E., Johnson, J. C., Saykally, R. & Yang, P. Nanowire dye-sensitized solar cells. *Nat Mater* **4**, 455-459, doi:10.1038/nmat1387 (2005).

- 11 Yu, X. *et al.* High Efficiency Organic/Silicon-Nanowire Hybrid Solar Cells: Significance of Strong Inversion Layer. *Sci Rep* **5**, 17371, doi:10.1038/srep17371 (2015).
- 12 Albrecht, S. *et al.* Monolithic perovskite/silicon-heterojunction tandem solar cells processed at low temperature. *Energy & Environmental Science* **9**, 81-88, doi:10.1039/c5ee02965a (2016).
- 13 Luque, A. & Hegedus, S. *Handbook of photovoltaics science and engineering*. 2 edn, (John Wiley & Sons, 2011).
- 14 Green, M. A. *Silicon Solar Cells Advanced Principles*. (1995).
- 15 Goetzberger, A., Knobloch, J. & Voss, B. *Crystalline Silicon Solar Cells*. (John Wiley & Sons Ltd, 1998).
- 16 Van Roosbroeck, W. Theory of the Flow of Electrons and Holes in Germanium and Other Semiconductors. (1950).
- 17 Baca, A. J. *et al.* Printable Single-Crystal Silicon Micro/Nanoscale Ribbons, Platelets and Bars Generated from Bulk Wafers. *Advanced Functional Materials* **17**, 3051-3062, doi:10.1002/adfm.200601161 (2007).
- 18 Yoon, J. *et al.* Ultrathin silicon solar microcells for semitransparent, mechanically flexible and microconcentrator module designs. *Nat Mater* **7**, 907-915, doi:10.1038/nmat2287 (2008).
- 19 Yablonovitch, E. Statistical Ray Optics. *Journal of the Optical Society of America* **72**, 899-907, doi:Doi 10.1364/Josa.72.000899 (1982).

- 20 Munday, J. N., Callahan, D. M. & Atwater, H. A. Light trapping beyond the  $4n^2$  limit in thin waveguides. (2012).
- 21 Yu, Z., Raman, A. & Fan, S. Fundamental limit of light trapping in grating structures. *Opt Express* **18 Suppl 3**, A366-380, doi:10.1364/OE.18.00A366 (2010).
- 22 Callahan, D. M., Munday, J. N. & Atwater, H. A. Solar Cell light trapping beyond the ray optic limit. *Nano Lett* **12**, 214-218, doi:10.1021/nl203351k (2012).
- 23 Yun, J. H. *et al.* Incident light adjustable solar cell by periodic nanolens architecture. *Sci Rep* **4**, 6879, doi:10.1038/srep06879 (2014).
- 24 Spinelli, P., Verschuuren, M. A. & Polman, A. Broadband omnidirectional antireflection coating based on subwavelength surface Mie resonators. *Nat Commun* **3**, 692, doi:10.1038/ncomms1691 (2012).
- 25 Wehrspohn, R. B. & Üpping, J. 3D photonic crystals for photon management in solar cells. *Journal of Optics* **14**, 024003, doi:10.1088/2040-8978/14/2/024003 (2012).
- 26 Zeng, L. *et al.* Efficiency enhancement in Si solar cells by textured photonic crystal back reflector. *Applied Physics Letters* **89**, 111111, doi:10.1063/1.2349845 (2006).
- 27 Ding, W. *et al.* Design of two dimensional silicon nanowire arrays for antireflection and light trapping in silicon solar cells. *Journal of Applied Physics* **115**, 014307, doi:10.1063/1.4848996 (2014).



- 28 Experimental Study of Design Parameters in Silicon Micropillar Array Solar Cells Produced by Soft Lithography and Metal-Assisted Chemical Etching.
- 29 Wang, K. X., Yu, Z., Liu, V., Cui, Y. & Fan, S. Absorption enhancement in ultrathin crystalline silicon solar cells with antireflection and light-trapping nanocone gratings. *Nano Lett* **12**, 1616-1619, doi:10.1021/nl204550q (2012).
- 30 Gjessing, J. *Photonic crystals for light trapping in solar cells*, University of Oslo, (2012).
- 31 Gjessing, J. *Photonic crystals for light trapping in solar cells* Philosophiae Doctor thesis, University of Oslo, (2011).
- 32 Han, S. E. & Chen, G. Toward the lambertian limit of light trapping in thin nanostructured silicon solar cells.
- 33 Ferry, V. E. *Light Trapping in Plasmonic Solar Cells*, California Institute of Technology, (2011).
- 34 Huang, Z. P. *et al.* Extended arrays of vertically aligned sub-10 nm diameter [100] Si nanowires by metal-assisted chemical etching. *Nano Letters* **8**, 3046-3051, doi:10.1021/nl802324y (2008).
- 35 Huang, Z. P., Geyer, N., Werner, P., de Boor, J. & Gosele, U. Metal-Assisted Chemical Etching of Silicon: A Review. *Advanced Materials* **23**, 285-308, doi:10.1002/adma.201001784 (2011).
- 36 Chong, T. K., Wilson, J., Mokkaṭpati, S. & Catchpole, K. R. Optimal wavelength scale diffraction gratings for light trapping in solar cells. *Journal of Optics* **14**, 024012, doi:10.1088/2040-8978/14/2/024012 (2012).

- 37 Mavrokefalos, A., Han, S. E., Yerci, S., Branham, M. S. & Chen, G. Efficient light trapping in inverted nanopyramid thin crystalline silicon membranes for solar cell applications. *Nano Lett* **12**, 2792-2796, doi:10.1021/nl2045777 (2012).
- 38 Kim, J. *et al.* Surface-concentrated light and efficient carrier collection in microhole-patterned Si solar cells. *Opt Express* **21 Suppl 4**, A607-615, doi:10.1364/OE.21.00A607 (2013).
- 39 Yu, K. J. *et al.* Light Trapping in Ultrathin Monocrystalline Silicon Solar Cells. *Advanced Energy Materials* **3**, 1401-1406, doi:10.1002/aenm.201300542 (2013).
- 40 Lee, S. M. *et al.* Printable nanostructured silicon solar cells for high-performance, large-area flexible photovoltaics. *ACS Nano* **8**, 10507-10516, doi:10.1021/nn503884z (2014).
- 41 Li, G., Li, H., Ho, J. Y., Wong, M. & Kwok, H. S. Nanopyramid structure for ultrathin c-Si tandem solar cells. *Nano Lett* **14**, 2563-2568, doi:10.1021/nl500366c (2014).
- 42 Karakasoglu, I., Wang, K. X. Z. & Fan, S. H. Optical-Electronic Analysis of the Intrinsic Behaviors of Nanostructured Ultrathin Crystalline Silicon Solar Cells. *Acs Photonics* **2**, 883-889, doi:10.1021/acsp Photonics.5b00081 (2015).
- 43 Weinstein, L. A., Hsu, W.-C., Yerci, S., Boriskina, S. V. & Chen, G. Enhanced absorption of thin-film photovoltaic cells using an optical cavity. *Journal of Optics* **17**, 055901, doi:10.1088/2040-8978/17/5/055901 (2015).

- 44 Branham, M. S. *et al.* 15.7% Efficient 10- $\mu\text{m}$ -thick crystalline silicon solar cells using periodic nanostructures. *Adv Mater* **27**, 2182-2188, doi:10.1002/adma.201405511 (2015).
- 45 Yan , X. *et al.* Enhanced Omnidirectional Photovoltaic Performance of Solar Cells Using Multiple-Discrete-Layer Tailored- and Low-Refractive Index Anti-Reflection Coatings. *Adv. Funct. Mater.* (2012).
- 46 Aroutiounian, V. M., Martirosyan, K. & Soukiassian, P. Almost zero reflectance of a silicon oxynitride/porous silicon double layer antireflection coating for silicon photovoltaic cells. *Journal of Physics D-Applied Physics* **39**, 1623-1625, doi:10.1088/0022-3727/39/8/022 (2006).
- 47 Gangopadhyay, U., Kim, K. H., Mangalaraj, D. & Yi, J. S. Low cost CBD ZnS antireflection coating on large area commercial mono-crystalline silicon solar cells. *Applied Surface Science* **230**, 364-370, doi:10.1016/j.apsusc.2004.02.059 (2004).
- 48 Dobrzański, L. A., Szindler, M., Drygała, A. & Szindler, M. M. Silicon solar cells with  $\text{Al}_2\text{O}_3$  antireflection coating.
- 49 Nagel, H., Aberle, A. G. & Hezel, R. Optimised antireflection coatings for planar silicon solar cells using remote PECVD silicon nitride and porous silicon dioxide. *Progress in Photovoltaics* **7**, 245-260, doi:Doi 10.1002/(Sici)1099-159x(199907/08)7:4<245::Aid-Pip255>3.3.Co;2-V (1999).
- 50 Schmidt, J., Kerr, M. & Cuevas, A. Surface passivation of silicon solar cells using plasma-enhanced chemical-vapour-deposited SiN films and thin thermal

- SiO<sub>2</sub>/plasma SiN stacks. *Semiconductor Science and Technology* **16**, 164-170, doi:Doi 10.1088/0268-1242/16/3/308 (2001).
- 51 Proust, J., Fehrembach, A. L., Bedu, F., Ozerov, I. & Bonod, N. Optimized 2D array of thin silicon pillars for efficient antireflective coatings in the visible spectrum. *Scientific Reports* **6**, doi:Artn 24947 10.1038/Srep24947 (2016).
- 52 Baryshnikova, K. V., Petrov, M. I., Babicheva, V. E. & Belov, P. A. Plasmonic and silicon spherical nanoparticle antireflective coatings. *Sci Rep* **6**, 22136, doi:10.1038/srep22136 (2016).
- 53 Yao, Y., Brueckner, E., Li, L. F. & Nuzzo, R. Fabrication and assembly of ultrathin high-efficiency silicon solar microcells integrating electrical passivation and anti-reflection coatings. *Energy & Environmental Science* **6**, 3071-3079, doi:10.1039/c3ee42230e (2013).
- 54 Raut, H. K., Ganesh, V. A., Nair, A. S. & Ramakrishna, S. Anti-reflective coatings: A critical, in-depth review. *Energy & Environmental Science* **4**, 3779-3804, doi:10.1039/c1ee01297e (2011).
- 55 Zhong, S., Zeng, Y., Huang, Z. & Shen, W. Superior broadband antireflection from buried Mie resonator arrays for high-efficiency photovoltaics. *Sci Rep* **5**, 8915, doi:10.1038/srep08915 (2015).
- 56 Boden, S. A. & Bagnall, D. M. Optimization of moth-eye antireflection schemes for silicon solar cells. *Prog. Photovolt: Res. Appl.* .

- 57 Brongersma, M. L., Cui, Y. & Fan, S. Light Management for Photovoltaics Using High-Index Nanostructures. *Nature Material* **13**, 451–460, doi:10.1038/nmat3921 (2014).
- 58 Boroumand, J., Das, S., Vazquez-Guardado, A., Franklin, D. & Chanda, D. Unified Electromagnetic-Electronic Design of Light Trapping Silicon Solar Cells. *Scientific Reports* **6**, doi:Artn 31013 10.1038/Srep31013 (2016).
- 59 Shir, D., Yoon, J., Chanda, D., Ryu, J. H. & Rogers, J. A. Performance of ultrathin silicon solar microcells with nanostructures of relief formed by soft imprint lithography for broad band absorption enhancement. *Nano Lett* **10**, 3041-3046, doi:10.1021/nl101510q (2010).
- 60 Shin, J. C. *et al.* Experimental Study of Design Parameters in Silicon Micropillar Array Solar Cells Produced by Soft Lithography and Metal-Assisted Chemical Etching. *Ieee Journal of Photovoltaics* **2**, 129-133, doi:10.1109/Jphotov.2011.2180894 (2012).
- 61 Balasundaram, K. *et al.* Porosity control in metal-assisted chemical etching of degenerately doped silicon nanowires. *Nanotechnology* **23**, doi:Artn 305304 10.1088/0957-4484/23/30/305304 (2012).
- 62 Hass, G. *et al.* *Physics of Thin Films*. Vol. 2 (Academic press, 1964).
- 63 Sah, R. E. *Silicon Nitride, Silicon Dioxide, and Emerging Dielectrics*. 11 edn, Vol. 35 (The Electrochemical Society, 2011).

- 64 Kelzenberg, M. D. *et al.* Enhanced absorption and carrier collection in Si wire arrays for photovoltaic applications. *Nature Materials* **9**, 239-244, doi:10.1038/nmat2635 (2010).
- 65 Wolden, C. A. *et al.* Photovoltaic manufacturing: Present status, future prospects, and research needs. *Journal of Vacuum Science & Technology A* **29**, 030801, doi:10.1116/1.3569757 (2011).
- 66 Frühauf, J., Gärtner, E. & Krönert, S. *Shape and Functional Elements of the Bulk Silicon Microtechnique*. 1 edn, (Springer-Verlag Berlin Heidelberg, 2005).
- 67 Petti, C., Newman, B., Brainard, R. & Li, J. Optimal thickness for crystalline silicon solar cells. 1-15 (2011).
- 68 Tool, C. J. J., Burgers, A. R., Manshanden, P., Weeber, A. W. & van Straaten, B. H. M. Influence of wafer thickness on the performance of multicrystalline Si solar cells: an experimental study. *Progress in Photovoltaics* **10**, 279-291, doi:10.1002/pip.421 (2002).
- 69 Wolf, M. Updating the Limit Efficiency of Silicon Solar-Cells. *Ieee Transactions on Electron Devices* **27**, 751-760, doi:Doi 10.1109/T-Ed.1980.19932 (1980).
- 70 Pillai, S., Catchpole, K. R., Trupke, T. & Green, M. A. Surface plasmon enhanced silicon solar cells. *Journal of Applied Physics* **101**, 093105, doi:10.1063/1.2734885 (2007).
- 71 Guo, X. *et al.* Two- and three-dimensional folding of thin film single-crystalline silicon for photovoltaic power applications. *Proc Natl Acad Sci U S A* **106**, 20149-20154, doi:10.1073/pnas.0907390106 (2009).

- 72 Corcoran, C. J. *et al.* Mechanisms of enhanced optical absorption for ultrathin silicon solar microcells with an integrated nanostructured backside reflector. *ACS Appl Mater Interfaces* **5**, 4239-4246, doi:10.1021/am400408g (2013).
- 73 Wang, Z. Y. *et al.* Broadband optical absorption by tunable Mie resonances in silicon nanocone arrays. *Sci Rep* **5**, 7810, doi:10.1038/srep07810 (2015).
- 74 Wang, S. *et al.* Large-area free-standing ultrathin single-crystal silicon as processable materials. *Nano Lett* **13**, 4393-4398, doi:10.1021/nl402230v (2013).
- 75 Fan, Z. *et al.* Ordered arrays of dual-diameter nanopillars for maximized optical absorption. *Nano Lett* **10**, 3823-3827, doi:10.1021/nl1010788 (2010).
- 76 Brongersma, M. L., Cui, Y. & Fan, S. H. Light management for photovoltaics using high-index nanostructures. *Nature materials* **13**, 451-460, doi:10.1038/Nmat3921 (2014).
- 77 Ko, M. D., Rim, T., Kim, K., Meyyappan, M. & Baek, C. K. High efficiency silicon solar cell based on asymmetric nanowire. *Sci Rep* **5**, 11646, doi:10.1038/srep11646 (2015).
- 78 Dewan, R., Jovanov, V., Hamraz, S. & Knipp, D. Analyzing periodic and random textured silicon thin film solar cells by Rigorous Coupled Wave Analysis. *Sci Rep* **4**, 6029, doi:10.1038/srep06029 (2014).
- 79 D. Shir, J. Yoon, D. Chanda, J. H. Ryu & Rogers, J. A. Performance of Ultrathin Silicon Solar Microcells with Nanostructures of Relief Formed by Soft Imprint Lithography for Broad Band Absorption Enhancement. *Nano Letters* **10**, 3041–3046 (2010).

- 80 Ki Jun Yu *et al.* Light Trapping in Ultra-thin Monocrystalline Silicon Solar Cells. *Advanced Energy Materials* **3**, 1401-1406 (2013).
- 81 Chen, Z., Pang, S. K., Yasutake, K. & Rohatgi, A. Plasma-enhanced chemical-vapor-deposited oxide for low surface recombination velocity and high effective lifetime in silicon. *Journal of Applied Physics* **74**, 2856, doi:10.1063/1.354638 (1993).
- 82 Bikbajevs, V., Grivickas, V., Linnros, J. & Tellefsen, J. A. Injection-level dependent surface recombination velocities at the Si-SiO<sub>2</sub> interface. *Physica Scripta* **T79**, 322-326, doi:DOI 10.1238/Physica.Topical.079a00322 (1999).
- 83 Grant, N. & McIntosh, K. in *Conference Proceedings Solar* (Australian Solar Energy Society, 2010).
- 84 Aberle, A. G., Glunz, S. & Warta, W. Impact of Illumination Level and Oxide Parameters on Shockley-Read-Hall Recombination at the Si-SiO<sub>2</sub> Interface. *Journal of Applied Physics* **71**, 4422-4431, doi:Doi 10.1063/1.350782 (1992).
- 85 Schultz, O., Glunz, S. W. & Willeke, G. P. SHORT COMMUNICATION: ACCELERATED PUBLICATION: Multicrystalline silicon solar cells exceeding 20% efficiency. *Progress in Photovoltaics: Research and Applications* **12**, 553-558, doi:10.1002/pip.583 (2004).
- 86 Cuevas, A. & Macdonald, D. Measuring and interpreting the lifetime of silicon wafers. *Solar Energy* **76**, 255-262, doi:10.1016/j.solener.2003.07.033 (2004).



- 87 Jensen, N. *et al.* Recombination mechanisms in amorphous silicon/crystalline silicon heterojunction solar cells. *Journal of Applied Physics* **87**, 2639, doi:10.1063/1.372230 (2000).
- 88 Pisarkiewicz, T. Photodecay method in investigation of materials and photovoltaic structures. *Opto-Electron Rev* **12**, 33-40 (2004).
- 89 Sinton, R. A. & Cuevas, A. Contactless determination of current-voltage characteristics and minority-carrier lifetimes in semiconductors from quasi-steady-state photoconductance data. *Applied Physics Letters* **69**, 2510-2512, doi:Doi 10.1063/1.117723 (1996).
- 90 Anner, G. E. *Planar processing primer*. (Van Nostrand Reinhold, 1990).
- 91 STEM, N. & CID, M. Studies of phosphorus Gaussian profile emitter silicon solar cells. *Materials Research* **4**, 143-148 (2001).
- 92 Shi, D., Zeng, Y. & Shen, W. Perovskite/c-Si tandem solar cell with inverted nanopyramids: realizing high efficiency by controllable light trapping. *Sci Rep* **5**, 16504, doi:10.1038/srep16504 (2015).
- 93 Jeong, S., McGehee, M. D. & Cui, Y. All-back-contact ultra-thin silicon nanocone solar cells with 13.7% power conversion efficiency. *Nat Commun* **4**, 2950, doi:10.1038/ncomms3950 (2013).
- 94 Kerr, M. J. & Cuevas, A. Very low bulk and surface recombination in oxidized silicon wafers. *Semiconductor Science and Technology* **17**, 35-38, doi:Doi 10.1088/0268-1242/17/1/306 (2002).

- 95 Jansen, H. V., de Boer, M. J., Unnikrishnan, S., Louwerse, M. C. & Elwenspoek, M. C. Black silicon method X: a review on high speed and selective plasma etching of silicon with profile control: an in-depth comparison between Bosch and cryostat DRIE processes as a roadmap to next generation equipment. *Journal of Micromechanics and Microengineering* **19**, doi:Artn 033001 10.1088/0960-1317/19/3/033001 (2009).